

RESEARCH ARTICLE

10.1002/2013JD021119

Key Points:

- Phase partitioning of cloud water in GCMs is investigated
- Cloud water phase in GCMs is compared to satellite observations
- Ice nucleation parameterization influence on cloud water phase is investigated

Correspondence to:

M. Komurcu,
mugekomurcu@gmail.com

Citation:

Komurcu, M., T. Storelvmo, I. Tan, U. Lohmann, Y. Yun, J. E. Penner, Y. Wang, X. Liu, and T. Takemura (2014), Intercomparison of the cloud water phase among global climate models, *J. Geophys. Res. Atmos.*, 119, 3372–3400, doi:10.1002/2013JD021119.

Received 30 OCT 2013

Accepted 18 FEB 2014

Accepted article online 24 FEB 2014

Published online 27 MAR 2014

Intercomparison of the cloud water phase among global climate models

Muge Komurcu¹, Trude Storelvmo¹, Ivy Tan¹, Ulrike Lohmann², Yuxing Yun^{3,4}, Joyce E. Penner³, Yong Wang^{5,6}, Xiaohong Liu^{5,6}, and Toshihiko Takemura⁷
¹Department of Geology and Geophysics, Yale University, New Haven, Connecticut, USA, ²Institute of Atmospheric and Climate Science, ETH Zurich, Zurich, Switzerland, ³Department of Atmospheric, Oceanic and Space Sciences, University of Michigan, Ann Arbor, Michigan, USA, ⁴Atmospheric and Oceanic Sciences Program, Princeton University/Geophysical Fluid Dynamics Laboratory, Princeton, New Jersey, USA, ⁵Department of Atmospheric Science, University of Wyoming, Laramie, Wyoming, USA, ⁶Pacific Northwest National Laboratory, Richland, Washington, USA, ⁷Research Institute for Applied Mechanics, Kyushu University, Fukuoka, Japan

Abstract Mixed-phase clouds (clouds that consist of both cloud droplets and ice crystals) are frequently present in the Earth's atmosphere and influence the Earth's energy budget through their radiative properties, which are highly dependent on the cloud water phase. In this study, the phase partitioning of cloud water is compared among six global climate models (GCMs) and with Cloud and Aerosol Lidar with Orthogonal Polarization retrievals. It is found that the GCMs predict vastly different distributions of cloud phase for a given temperature, and none of them are capable of reproducing the spatial distribution or magnitude of the observed phase partitioning. While some GCMs produced liquid water paths comparable to satellite observations, they all failed to preserve sufficient liquid water at mixed-phase cloud temperatures. Our results suggest that validating GCMs using only the vertically integrated water contents could lead to amplified differences in cloud radiative feedback. The sensitivity of the simulated cloud phase in GCMs to the choice of heterogeneous ice nucleation parameterization is also investigated. The response to a change in ice nucleation is quite different for each GCM, and the implementation of the same ice nucleation parameterization in all models does not reduce the spread in simulated phase among GCMs. The results suggest that processes subsequent to ice nucleation are at least as important in determining phase and should be the focus of future studies aimed at understanding and reducing differences among the models.

1. Introduction

According to the *Intergovernmental Panel on Climate Change* [2013], cloud feedbacks continue to be the largest source of uncertainty in GCM estimates of Earth's climate sensitivity. Clouds can consist of liquid water droplets (liquid clouds) or ice crystals (ice clouds). Furthermore, at temperatures between -38°C and 0°C , clouds can be of mixed phase, meaning that both cloud droplets (liquid water) and ice crystals may coexist and influence the cloud radiative and thermodynamic properties [e.g., Fridlind *et al.*, 2012]. Subsequently, GCM simulations of cloud feedback are sensitive to the treatment of cloud water phase (liquid water or ice) [e.g., Li and Le Treut, 1992; Mitchell *et al.*, 1989]. Mixed-phase clouds are a significant component of the atmosphere with an average global coverage of 20 to 30% [Warren *et al.*, 1988]. This number is likely to change as the atmosphere warms in response to increasing greenhouse gas concentrations. Therefore, a good representation of the phase partitioning of the cloud water content between cloud liquid and cloud ice in global climate models (GCMs) is crucial for the correct simulation of cloud feedback and in turn the influence of clouds on the current and future climate.

At subzero temperatures, the equilibrium vapor pressure difference between ice and liquid water allows for the growth of ice crystals at the expense of evaporating cloud droplets if the ambient vapor pressure is between saturation with respect to water and ice, a process known as the Wegener-Bergeron-Findeisen (WBF) process [Wegener, 1911; Bergeron, 1935; Findeisen, 1938]. The WBF process can thus lead to rapid conversion of liquid to ice, with associated changes to cloud radiative properties and precipitation release. However, the process only comes into play once a few ice crystals have nucleated in an otherwise liquid cloud. As a result, the liquid water contents of mixed-phase clouds are dependent on the processes of ice crystal nucleation, growth, and removal rates. Modeling the partitioning between the cloud liquid and cloud

ice has been a challenge due to the unknowns related to the cloud ice processes and especially ice nucleation. These microphysical processes have also been proven difficult to measure both in the laboratory and in the field over the years [e.g., *DeMott et al.*, 2011]. Furthermore, until recently, the lack of accurate satellite retrievals of the phase of the cloud hydrometeors made it difficult to constrain the models using observations, which has further contributed to the challenge [e.g., *Waliser et al.*, 2009]. Another contribution to this challenge is the coarse grid size of the GCMs, which makes it difficult to represent the subgrid scale cloud processes [e.g., *Menon et al.*, 2003]. Efforts have been made recently to combine theory, laboratory, and in situ measurements to develop realistic parameterizations of nucleation, growth, and precipitation of ice crystals [e.g., *Phillips et al.*, 2008; *DeMott et al.*, 2010; *Hoose et al.*, 2010; *McFarquhar et al.*, 2011].

In this study, we concentrate on one of the key factors controlling the phase partitioning in mixed-phase clouds: ice nucleation. Ice nucleation determines the number of ice crystals formed and in turn can affect the rate of growth and precipitation of the crystals, leading to differences in cloud water phase. Ice nucleation can take place both homogeneously, from small solution droplets at temperatures below -38°C , and heterogeneously, with the aid of available ice nuclei at temperatures below approximately -4°C [*Pruppacher and Klett*, 1997]. In this study, we are mainly interested in the temperature range of 0 to -38°C in which ice formation occurs by heterogeneous freezing processes only. In this temperature range, the low abundance of ice nuclei in the atmosphere allows for both cloud water phases (ice crystals and cloud droplets) to coexist yielding mixed-phase clouds. Therefore, when discussing ice nucleation in the remainder of this study, we will be referring to heterogeneous ice nucleation processes.

There are various proposed ice nucleation parameterizations available for use in GCMs based on laboratory studies or in situ measurements [e.g., *Meyers et al.*, 1992; *Lohmann and Diehl*, 2006; *DeMott et al.*, 2010; *Hoose et al.*, 2010]. Changing the ice nucleation mechanism used in a GCM can lead to differences in the model-predicted ice and liquid water paths and cloud radiative forcing, which may result in different radiative fluxes and climate sensitivities compared to the default ice nucleation parameterizations of the models [e.g., *DeMott et al.*, 2010; *Storelvmo et al.*, 2011; *Yun and Penner*, 2013; *Xie et al.*, 2013]. These changes take place in the following manner: A change in the ice nucleation parameterization can change the number of nucleated ice crystals, which then leads to changes in the WBF process. Depending on the growth rate, mass and size of the crystals can change leading to differences in the precipitation rate. As a result, the rate of nucleation, growth, and precipitation of ice crystals can influence the liquid and ice water mass remaining in the cloud, leading to changes in cloud radiative properties and to different sensitivities to increasing anthropogenic aerosols and to increasing temperatures under climate change. Furthermore, ice precipitation efficiencies, growth rates of ice crystals through the WBF process, and riming depend on subgrid scale processes and therefore are not well represented in GCMs [e.g., *Fan et al.*, 2011]. For example, the shapes of crystals formed depend on the environmental conditions at the vicinity of the ice formation and determine the growth rates of the crystals through gradients of fluxes on different crystal faces [e.g., *Fukuta and Takahashi*, 1999]. Fall velocities of ice crystals also change depending on their shape resulting in some crystal shapes to stay longer in cloud and have more time for growth depleting the cloud droplets [e.g., *Avramov and Harrington*, 2010]. Most GCMs assume spherical ice crystals to avoid these problems. Furthermore, precipitation and water paths in GCMs are also sensitive to the criteria assumed in the autoconversion rates (i.e., the critical particle cutoff diameter) of hydrometeors (i.e., pristine ice to snow) [*Gottelman et al.*, 2010].

Several GCM intercomparison studies have been carried out over the years, though none of them concentrated on the phase partitioning of cloud water. These studies showed differences in both the spatial structure and magnitude of liquid and ice water paths simulated by different GCMs as well as compared to satellite observations [e.g., *Penner et al.*, 2006; *Waliser et al.*, 2009; *Eliasson et al.*, 2011; *Jiang et al.*, 2012]. For example, *Jiang et al.* [2012] compared the GCM results of the Phase 5 of the Coupled Model Intercomparison Project (CMIP5) to Phase 3 (CMIP3) and found that both ice and liquid water paths have improved for most of the models as a result of model development. Furthermore, several of the GCM intercomparison studies concentrated on the aerosol indirect effect. *Penner et al.* [2006] investigated the influence of the changes in liquid cloud processes (i.e., the autoconversion scheme and cloud droplet number parameterization) on the model-predicted ice and liquid water paths as well as the aerosol indirect effect. *Quaas et al.* [2009] compared the aerosol indirect effects of liquid stratiform clouds, while *Gottelman et al.* [2012] focused on ice clouds using two GCMs. Most studies concentrate on validating and comparing models based on the integrated amount of liquid and/or ice in the atmospheric column. In mixed-phase clouds, however, the radiative and

Table 1. Description of the GCMs Used in This Study^a

GCMs	Resolution	Vertical Levels	Heterogeneous Ice Nucleation Parameterization	Aerosol Module	Aerosol Emissions
ECHAM6	2.8° × 2.8°	31	<i>Lohmann and Diehl</i> [2006] <i>Diehl et al.</i> [2006]	7 Modes [<i>Stier et al.</i> , 2005]	AeroCom [<i>Dentener et al.</i> , 2006]
CAM-IMPACT	1.9° × 2.5°	26	<i>Phillips et al.</i> [2008] <i>Young</i> [1974]	12 Modes [<i>Liu et al.</i> , 2005]	[<i>Wang et al.</i> , 2009]
CAM-Oslo	1.9° × 2.5°	26	<i>Hoose et al.</i> [2010]	12 Modes [<i>Seland et al.</i> , 2008]	AeroCom [<i>Dentener et al.</i> , 2006]
CAM5.1 MAM3	1.9° × 2.5°	30	<i>Meyers et al.</i> [1992] <i>Young</i> [1974] <i>Liu et al.</i> [2007]	3 Modes [<i>Liu et al.</i> , 2012]	IPCC AR5 [<i>Lamarque et al.</i> , 2010]
CAM5.1 MAM7	1.9° × 2.5°	30	<i>Meyers et al.</i> [1992] <i>Young</i> [1974] <i>Liu et al.</i> [2007]	7 Modes [<i>Liu et al.</i> , 2012]	IPCC AR5 [<i>Lamarque et al.</i> , 2010]
SPRINTARS	1.12° × 1.12°	30	<i>Lohmann and Diehl</i> [2006] <i>Diehl et al.</i> [2006]	7 Modes [<i>Takemura et al.</i> , 2000, 2002, 2005]	AeroCom [<i>Dentener et al.</i> , 2006]

^aIPCC AR5: The fifth assessment report of the Intergovernmental Panel on Climate Change.

thermodynamic properties of the clouds depend on the partitioning between cloud liquid water and cloud ice crystals. Hence, the goals of this study are to show the differences in the simulated cloud water phase in GCMs and to point out the importance of the cloud ice processes on the correct representation of cloud water phase in models. We first intercompare the output of six GCMs and compare them against satellite observations focusing on cloud water phase. Next, we examine one of the key processes affecting cloud water phase, the influence of heterogeneous ice nucleation parameterizations on the GCM-simulated cloud water phase. To analyze the sensitivity of the cloud water phase to ice nucleation parameterization, we perform two experiments. In the first experiment, we perform multiyear simulations using the default setup of the models, whereas in the second experiment, we fix the ice nucleation mechanism in each GCM to the parameterization presented by *DeMott et al.* [2010]. Finally, we perform the same sets of experiments with preindustrial aerosol emissions to evaluate the sensitivity of the total anthropogenic aerosol effect to the choice of heterogeneous ice nucleation parameterization. In section 2, we describe the six GCMs used in this intercomparison and present the observational data sets used for our analysis. We explain the experimental setup of the GCMs in section 3. In section 4, we present results of the experiments and compare the results of the two experiments. In section 5, we present our conclusions.

2. Description of the GCMs and Observational Data

In this study, we analyze cloud water properties from six GCMs. To compare model results with observations, we use satellite observations from Cloud and Aerosol Lidar with Orthogonal Polarization (CALIOP), Moderate Resolution Imaging Spectroradiometer (MODIS), CloudSat, and International Satellite Cloud Climatology Project (ISCCP). Using satellite data products in comparison with model output requires caution due to the uncertainties associated with satellite retrievals. Some areas of challenge that pose uncertainties in the satellite algorithms determining water contents of clouds are the separation of drizzle (or falling ice) from cloud droplets (or suspended ice crystals), the determination of cloud phase in mixed-phase clouds, and the use of algorithms that employ cloud top particle size distributions in estimating cloud layer height [*Stephens et al.*, 2002; *Waliser et al.*, 2009]. In this section, we describe each model, with a focus on its treatment of aerosol and cloud microphysics, as well as the observational data sets and uncertainties related to their retrieval. The details of the GCMs contributing to this study are listed in Table 1.

2.1. Community Atmosphere Model Version 5.1 Using a Modal Aerosol Scheme With Seven Lognormal Modes (CAM 5.1 MAM7)

This is the National Center for Atmospheric Research (NCAR) Community Atmosphere Model (CAM), version 5.1. In the model version used here, aerosols are represented using a modal aerosol scheme with seven lognormal modes (MAM7): Aitken, accumulation, fine dust, coarse dust, fine sea salt, coarse sea salt, and primary carbon [*Liu et al.*, 2012]. Both mass and number concentrations of liquid water and ice phases of the

stratiform clouds are predicted [Morrison and Gettelman, 2008]. There is a subgrid representation of liquid water but not for ice. Heterogeneous ice nucleation processes included are deposition-condensation freezing, contact freezing, and immersion freezing [Liu et al., 2007]. Deposition-condensation nucleation is calculated according to Meyers et al. [1992]. Immersion freezing is assumed implicit in Meyers et al. [1992] parameterization of deposition-condensation freezing [Gettelman et al., 2010]. Contact freezing follows the parameterization by Young [1974], and the concentration of contact ice nuclei (IN) is calculated using the model-predicted coarse mode dust. Secondary ice nucleation through the Hallet-Mossop process is also included in the model and follows Cotton et al. [1986]. A modified version of the approach by Rotstajn et al. [2000] is used to represent the WBF process [Gettelman et al., 2010].

2.2. CAM 5.1 MAM3

This model is the same as CAM5.1-MAM7 except that it uses a three lognormal mode aerosol scheme (MAM3), which includes the Aitken, accumulation, and coarse modes but does not have separate modes for dust and sea-salt aerosols. Contact IN are assumed to be dust aerosols, and their number concentration is calculated as a fraction of the coarse mode aerosols.

2.3. CAM-Oslo

This model is an extended version of NCAR's third generation of CAM, CAM3, and includes a sophisticated aerosol life cycle module with a hybrid modal/size bin representation forming the CAM-Oslo model. The module treats sea-salt, mineral dust, sulfate, black carbon (BC), and organic aerosols. Their size distributions are described by 12 lognormal modes and 44 size bins with process-determined mixing states [Seland et al., 2008]. The aerosol module was combined with NCAR CAM3 with two-moment cloud microphysics following Storelvmo et al. [2006, 2008a] and utilized for a range of studies of aerosol effects on clouds and climate. Heterogeneous ice nucleation follows a semiempirical parameterization based on classical nucleation theory [Hoose et al., 2010]. Immersion, contact, and deposition freezing on mineral dust and soot particles are included for the purpose of this study. Secondary ice nucleation through the Hallet-Mossop process follows Levkov et al. [1992], and the WBF process follows the subgrid scale treatment described in Storelvmo et al. [2008b, 2010].

2.4. CAM-IMPACT

This GCM is a coupled model with two components: an enhanced version of NCAR CAM3, which follows both the number and mass concentrations of hydrometeors, and the University of Michigan IMPACT aerosol model. The IMPACT model treats a total of 12 aerosol types and/or size bins: three sizes representing the number and mass of pure sulfate aerosols (i.e., nucleation, Aitken, and accumulation modes), one fossil/biofuel soot mode (but note Yun et al. [2013]), one biomass soot mode, four dust sizes, and four sea-salt sizes. Soot here refers to mixed organic/black carbon particles. All these aerosols may mix with sulfate through condensation and coagulation processes or through sulfate formation in cloud drops. Heterogeneous ice nucleation processes included in the model are the deposition-condensation nucleation, which is parameterized according to the Phillips et al. [2008] scheme, and contact freezing, which uses the updated Young [1974] parameterization [Yun and Penner, 2012]. The potential deposition-condensation ice nuclei for Experiments 1 and 2 are dust and soot but for Experiment 2 the potential ice nuclei are limited to those particles larger than 0.5 μm following their lognormal size distributions. Note that model results are improved with inclusion of ice nucleation on organic particles from marine sources [Yun and Penner, 2013]. The potential contact ice nuclei are also dust and soot particles. The adjustment to the Young [1974] parameterization was done to account for the fact that the number concentration of contact ice nuclei was determined by Young [1974] to be 0.2 cm^{-3} at -4°C in winter in Massachusetts, so the number concentrations of the dust and soot contact IN at -4°C at sea level are adjusted to 0.2 cm^{-3} at the same location and season. Also, dust contact IN are assumed to be 10 times more efficient than soot contact IN to account for the higher ice nucleation efficiency of dust. Aerosol sizes affect contact freezing through Brownian aerosol diffusivity. Secondary ice nucleation through the Hallet-Mossop process follows Cotton et al. [1986]. The Rotstajn et al. [2000] parameterization is used for the WBF process of ice growth.

2.5. European Centre/Hamburg Version 6 (ECHAM6)

The version of European Centre/Hamburg (ECHAM) used in this study is the sixth generation of the model developed by the Max Planck Institute for Meteorology, initially modifying the European Centre for Medium-Range Weather Forecasts (hence named EC) [Stevens et al., 2013]. It has a two-moment aerosol scheme (HAM) that predicts mass and number concentrations of sulfate, black carbon, particulate organic matter, mineral

dust, and sea salt using seven lognormal modes [Stier *et al.*, 2005]. Contact and immersion freezing are the heterogeneous ice nucleation mechanisms included in the model: Immersion ice nuclei include internally mixed dust and BC aerosols, and contact ice nuclei include externally mixed dust particles [Lohmann and Diehl, 2006; Lohmann *et al.*, 2007; Lohmann and Hoose, 2009]. Contact freezing depends on the aerosol diffusivity, number of contact IN, and temperature, and immersion freezing depends on number of immersion IN and temperature [Lohmann and Diehl, 2006]. For both contact and immersion freezing, to obtain the number of IN, each aerosol type is multiplied by a temperature-dependent relationship specific to the aerosol, which is obtained from laboratory studies [Lohmann and Diehl, 2006]. Secondary ice nucleation through the Hallett-Mossop is parameterized based on Levkov *et al.* [1992]. The WBF process is parameterized according to Korolev and Mazin [2003] taking the turbulent vertical velocity into account [Lohmann and Hoose, 2009].

2.6. Spectral Radiation Transport Model for Aerosol Species (SPRINTARS)

The Spectral Radiation Transport Model for Aerosol Species (SPRINTARS) is an aerosol scheme in the Model For Interdisciplinary Research on Climate (MIROC) developed by the Division of Climate System Research in the Atmosphere and Ocean Research Institute at the University of Tokyo, the National Institute for Environmental Studies in Japan, and the Research Institute for Global Change in the Japan Agency for Marine-Earth Science and Technology [Takemura *et al.*, 2005, 2009]. We will refer to this GCM as SPRINTARS in the remainder of this study. The model predicts mass mixing ratios of soil dust, BC, organic carbon, sulfate, sea salt, sulfur dioxide, and dimethylsulfide. Both soil dust and BC can act as IN, and ice nucleation takes place through contact and immersion freezing, which are parameterized according to Lohmann and Diehl [2006] and Diehl *et al.* [2006]. Both immersion and contact freezing are considered for SPRINTARS similar to ECHAM6. The number of IN is determined using a temperature-dependent relationship, which is obtained from a compilation of laboratory data, specific to the aerosol type as in Lohmann and Diehl [2006]. Contrary to ECHAM6, dust and BC can act as both contact and immersion IN. The secondary ice production through the Hallett-Mossop process is not included in this model. The WBF process is parameterized according to Wilson and Ballard [1999].

2.7. CALIOP

Data from the Cloud and Aerosol Lidar with Orthogonal Polarization (CALIOP) instrument on board the Cloud-Aerosol Lidar and Infrared Pathfinder Satellite Observation (CALIPSO) satellite, which was launched in April 2006, are the principal observational data set used in this study. CALIPSO flies in orbital formation with the A-train constellation of satellites. CALIOP is a two-wavelength (532 and 1064 nm) lidar with dual polarization receiver channels at 532 nm and a 1064 nm return signal channel; thus, it can discriminate between spherical and nonspherical particles [Winker *et al.*, 2009]. It is the first polarization lidar in space and hence offers powerful retrievals that can be used to obtain vertically resolved measurements of the thermodynamic phase of clouds. All the satellites of the A-train are in a 705 km altitude Sun-synchronous polar orbit with an equator-crossing time of about 1:30 P.M., local solar time, and a 16 day repeat cycle [Hunt *et al.*, 2009]. The vertical profiles of cloud thermodynamic phase from the CALIOP level-2 vertical feature mask (version 3) with data compiled from 2008 to 2011 are used in this study. The lidar has a sampling resolution of 335 m in the horizontal and 30 m in the vertical [Winker *et al.*, 2009].

Using regions of enhanced signal in attenuated backscatter profiles, the CALIOP layer detection algorithm first finds features (i.e., clouds, aerosols, surface, subsurface, and stratospheric level) [Winker *et al.*, 2009]. The type of feature is determined next using both optical (attenuated backscatter, color ratio, and volume depolarization ratio) and physical properties (i.e., altitude and latitude) followed by aerosol subtyping and cloud phase determination [Omar *et al.*, 2009; Hu *et al.*, 2009]. Using the cloud aerosol discrimination algorithm (CAD), a feature is characterized as either aerosol or cloud based on a confidence function that depends on multidimensional probability density functions (PDFs) of occurrence of clouds and aerosols [Liu *et al.*, 2009]. Only medium and high CAD confidence scores are used in this study to minimize misclassification of aerosols as clouds. A misclassification of aerosol into cloud can occur for about 1% of the total cloud and aerosol features, and most occurrences are at low altitudes (D. M. Winker, personal communication, 2014). Cloud phase is first determined using the layer-integrated depolarization ratio as liquid water, randomly oriented ice, and horizontally oriented ice [Hu *et al.*, 2009]. If aerosols are misclassified as clouds, determination of cloud phase through depolarization ratio will characterize the layer as either liquid water or ice. Next, spatial coherence correlation between depolarization ratio and backscatter is used to identify horizontally oriented ice particles mistakenly characterized as liquid water [Hu *et al.*, 2009]. We only use nighttime data to minimize spurious

results because the signal-to-noise ratio is lower for daytime retrievals (due to the fact that CALIOP's polarized beam at 532 nm is in the visible wavelength range). For multilayer clouds, a phase correction is made using temperature, depolarization ratio, and other cloud top climatology [Hu *et al.*, 2009]. Finally, particles classified as ice in clouds warmer than 0° C are reclassified as liquid, and particles in clouds colder than −40°C are reclassified as ice [Hu *et al.*, 2009]. This happens infrequently, less than 1% of the time (D. M. Winker, personal communication, 2014). Most of the errors in classification of ice and water phase are thought to occur due to the regions where the liquid water and ice branches overlap in depolarization plots. Spatial correlation method used in these cases can produce erroneous results if the noise is too large. For a mixed-phase single cloud layer, algorithm either reports ice or liquid and phase determination below deep cirrus clouds can be incorrect at times. Though, often correct classification is made, it is not clear how frequently these errors occur (D. M. Winker, personal communication, 2014). Because of the difficulties related to the multiple scattering characteristics of water clouds, the nondepolarization of horizontally oriented ice particles, and the computational expense of validating the multiple scattering of nonuniform particles in clouds, there are still uncertainties in differentiating the water phase in CALIOP despite the renewed phase determination algorithm [Hu *et al.*, 2009].

Following the approach of Choi *et al.* [2010], to match the observed cloud thermodynamic phase at a given height with the corresponding atmospheric temperatures, the National Center for Environmental Prediction–NCAR Reanalysis-2 data are used along with the CALIOP data. Reanalysis data also have internal errors mainly described in Kanamitsu *et al.* [2002]. We expect the uncertainties in temperature data from Reanalysis-2 to be minimal except for the regions of strong temperature inversions such as the Arctic. As explained in Choi *et al.* [2010], because we are using the cloud top heights measured by CALIOP and calculating cloud top temperature using the Reanalysis-2 temperature based on these heights, we do not expect any errors due to the use of Reanalysis-2.

2.8. MODIS

The Moderate Resolution Imaging Spectroradiometer (MODIS) is a 36-band spectroradiometer measuring visible and infrared radiation to collect various different observations flying on two A-train satellites: Terra and Aqua [King *et al.*, 2003]. We are using the liquid water path (LWP), ice water path (IWP), and cloud fraction data from MODIS on the Aqua satellite, which was launched in 2002. We calculate the 5 year mean LWP and IWP using the daily data from Collection 005 level-3 MYD08-D3 product [King *et al.*, 2003; Hubanks *et al.*, 2008] between 2004 and 2008. This product is derived from level-2 MODIS products and is given in 1° × 1° grid cells [King *et al.*, 2003]. Because MODIS provides in cloud LWP and IWP while the GCMs report grid box mean IWP and LWP, we multiply the LWP (IWP) data with the cloud fractions for liquid (ice) clouds to be consistent with model results as in Jiang *et al.* [2012].

MODIS also provides the pixel-level uncertainty of the daily retrievals of LWP and IWP from component error sources inherent to the retrievals [Platnick *et al.*, 2004]. These error sources include the incomplete knowledge of the instrument calibration, surface spectral albedo, and spectral atmospheric correction, the latter mainly due to moisture [Platnick *et al.*, 2004]. Reported pixel-level uncertainties provide the minimum baseline uncertainty and are calculated assuming that errors are perfectly correlated on a single day and uncorrelated day to day (R. Pincus, personal communication, 2014). Other uncertainties not quantified in these estimates are those related to one dimensionality of the models used to interpret observed radiances, vertical/horizontal inhomogeneity, multilayer cloud systems, non-plane-parallel cloud radiative effects, and cloud model assumptions such as ice crystal habits and particle size distributions [Platnick *et al.*, 2004]. For the time period used in this study, the median uncertainty is a factor of 0.3 for both LWP and IWP and maximum uncertainties are a factor of 0.8 for IWP and LWP, respectively. Jiang *et al.* [2012] assume that the uncertainties in the same data sets are a factor of 2, which may be reasonable when the nonquantified error sources are included.

2.9. CloudSat

CloudSat is an A-train constellation satellite that flies the first spaceborne millimeter wavelength cloud profiling radar with a 500 m vertical resolution and aims to provide information on the vertical cloud structure [Stephens *et al.*, 2002]. In this study, we use the ice water path obtained from the level-2 product (2B-CWC-RO), which is derived from the radar reflectivities (level-1 products) [Stephens *et al.*, 2002]. IWP data from 2006 to 2009 are used in this study. CloudSat ice water content (IWC) was found to be within 25% of in

situ measurements; however, some values exceeded this range, so *Waliser et al.* [2009] assigned a value of 40% for the systematic error [Austin et al., 2009; Waliser et al., 2009]. Some of the sources of uncertainties in retrievals are related to the particle size distributions, shapes of the ice crystals, and scattering of the nonspherical particles [Heymsfield et al., 2008]. Another uncertainty comes from the temperature-dependent determination of the phase [Eliasson et al., 2011]. Particles are characterized as ice at temperatures below -20°C , liquid above 0°C , and a combination of both phases in between [Waliser et al., 2009]. For additional information on uncertainties, see Heymsfield et al. [2008].

2.10. ISCCP

The International Satellite Cloud Climatology Project (ISCCP) data set is a collection of infrared and visible radiances (0.6 and $11\text{ }\mu\text{m}$) from international weather satellites since 1983 [Rossow and Schiffer, 1999]. Because of the sensitivity of the wavelengths of ISCCP to smaller particles, ISCCP is assumed to provide information on nonprecipitating ice mass and in fact provides a better match with CloudSat IWP without precipitation [Eliasson et al., 2011]. We calculate the LWP and IWP from the ISCCP data sets. The ISCCP provides the IWP and LWP separated into different cloud types. In this study, using the same method as in Storelvmo et al. [2008a], the IWP from cirrus, cirrostratus, deep convective clouds, and the ice fraction of altostratus, altocumulus, nimbostratus, cumulus, stratocumulus, and stratus clouds contribute to the calculation of the IWP [Rossow and Schiffer, 1999]. As in Storelvmo et al. [2008a], while calculating the water paths, one third of the total water path is assumed to be liquid water for deep convective clouds in the tropics. Data from 1983 to 2008 are used in this study. Cloud water phase in ISCCP is determined from the cloud top temperature. If cloud top temperature is below -13°C , the cloud is characterized as an ice cloud. This leads to uncertainties in the IWP for cases where liquid cloud layers exist beneath the cloud top [e.g., Waliser et al., 2009]. Water paths are obtained from optical thickness assuming a constant effective particle radius and a constant size distribution variance [Lin and Rossow, 1996]. Therefore, uncertainties result from optical thickness retrievals and assumptions in microphysical properties used in converting optical thickness to water paths [Lin and Rossow, 1996]. The uncertainty related to cloud type classification is found to be around 0.15 [Rossow and Schiffer, 1999]. For additional details in uncertainties, see Lin and Rossow [1996] and Rossow and Schiffer [1999].

3. Experiment Setup

We first concentrate on the differences in the model-simulated cloud water phase, water paths, and other fields through an experiment using the default settings of each GCM. Hence, in Experiment 1, each model is run using its default heterogeneous ice nucleation parameterizations that are described in section 2. We next focus on one of the factors influencing the phase partitioning of cloud water: heterogeneous ice nucleation parameterizations in the GCMs. To analyze the sensitivity of the GCM-simulated cloud water phase and other fields to the parameterization of ice nucleation, we perform a second experiment, in which we fix the ice nucleation parameterization for mixed-phase clouds in each GCM. In Experiment 2, the default ice nucleation parameterizations of the models are replaced with the parameterization of DeMott et al. [2010] for mixed-phase clouds. We choose the DeMott et al. [2010] parameterization because it is a parameterization obtained from in situ measurements of IN concentrations over a wide range of ambient conditions, regions, and seasons. It nucleates ice crystals based on model-predicted particle concentrations rather than assuming a number concentration of ice nuclei based on supersaturation or temperature while ignoring the spatial and temporal variations in IN. It is also relatively easy to implement in models.

DeMott et al. [2010] parameterize the active ice nuclei concentration (n_{IN} [L^{-1}]) based on a temperature-dependent relationship using the number concentration of model-predicted aerosol particles greater than $0.5\text{ }\mu\text{m}$ ($n_{\text{aer},0.5}$ [cm^{-3}]):

$$n_{\text{IN}} = a(273.16 - T_k)^b (n_{\text{aer},0.5})^{(c(273.16 - T_k) + d)} \quad (1)$$

In equation (1), T_k is the cloud temperature in Kelvin, and a , b , c , and d are empirical constants with values 0.0000594, 3.33, 0.0264, and 0.0033, respectively. The two experiments are depicted in Table 2, and each set of simulations was run for 5 years.

Because the radiative properties of the clouds and the way they respond to temperature changes in the atmosphere and at the surface changes depending on the partitioning of liquid water and ice crystals in the

Table 2. Description of the Two Simulated Cases

Simulation Name	Case Description
Experiment 1	Default model heterogeneous ice nucleation parameterizations are used for all models.
Experiment 2	Default heterogeneous ice nucleation parameterizations are replaced with <i>DeMott et al.</i> [2010] parameterization for all models for mixed-phase clouds.

clouds, it is crucial to simulate a realistic cloud phase for mixed-phase clouds in order to simulate cloud-climate feedback correctly. We therefore use supercooled liquid fraction (SLF) to quantify the cloud water phase partitioning. To analyze and compare the differences in cloud water phase among GCMs and between GCMs and CALIOP observations, we calculate the SLF as described in equation (2).

$$\text{SLF} = \frac{r_{\text{liquid water}}}{r_{\text{liquid water}} + r_{\text{ice}}} \quad (2)$$

In equation (2), r represents the mixing ratio in kg/kg. SLF is calculated in the models on six isotherms: -10°C , -15°C , -20°C , -25°C , -30°C , and -35°C . SLF from the GCMs is only sampled at cloud tops to be consistent with the clouds that would be observed by CALIOP, with the exception of optically thin (optical thickness less than 3) cloud tops, in which case lower cloud layers are included.

We determine the observed SLF using the footprints of liquid water and ice crystals from CALIOP data averaged over $2.5^{\circ} \times 2.5^{\circ}$ latitude-longitude grid boxes covering the globe using equation (3).

$$\text{SLF} = \frac{f_{\text{liquid water}}}{f_{\text{liquid water}} + f_{\text{randomly oriented ice}} + f_{\text{horizontally oriented ice}}} \quad (3)$$

In equation (3), f represents the number of footprints of ice crystals or liquid water. SLF data on isotherms are then obtained using the temperature from the NCEP/NCAR reanalysis data along with the cloud heights from CALIOP as in *Choi et al.* [2010]. The CALIOP algorithm can determine the phase of the cloud, as either liquid or ice (horizontally and vertically oriented), and it does not have a separate mixed-phase category. The frequency of the occurrence of ice and liquid water is obtained in smaller footprints (90 m horizontally at the Earth's surface with a vertical resolution of 30 m) [Hu et al., 2009] in CALIOP than the large grid sizes [$\sim 2.5^{\circ} \times 2.5^{\circ}$] of the GCMs. Thus, when calculating SLF from CALIOP, thousands of footprints are taken into account while averaging over a GCM grid size, making the SLF a good approximation to compare with the GCM-predicted SLF regardless of the lack of an explicit mixed-phase category in CALIOP. As a result, the higher resolution of the footprints of ice and liquid water obtained from CALIOP allows us to make the comparison of SLF between the GCMs and observations despite the fact that SLF from CALIOP is a frequency fraction and the SLF from the GCMs are mass fractions. It is important to note that CALIOP overpasses the same location every 16 days. Therefore, CALIOP does not provide a homogeneous coverage of data as we obtain from the models. When using CALIOP to validate model results, it is important to remember the uncertainties in the retrieval algorithms as explained in section 2. Currently, there is also lack of quantitative validations of CALIOP observations with aircraft or in situ measurements. Using only nighttime data from CALIOP can also lead to differences compared to the averaging in GCMs. Despite these uncertainties, the CALIOP data set is the best available global observational data set on cloud phase and is therefore used for model validation in this study.

For both experiments, all six GCMs are run using the preindustrial and the present-day aerosol emissions as listed in Table 1.

4. Results

4.1. Results of the Default Model Experiment (Experiment 1)

To analyze the differences in GCMs, we first provide results from the two-dimensional annual mean fields obtained from multiyear means. Figures 1 and 2 show the LWP and IWP for all six GCMs along with satellite observations. It is important to note that there are many factors contributing to uncertainties in satellite data sets, and these uncertainties can be quite large as explained in section 2. We use satellite data sets to validate GCM results bearing in mind the associated uncertainties in the retrieval algorithms along with the diurnal sampling and trajectories of satellite observations that could lead to differences compared with the sampling of the fields in GCMs. Based on these two figures, the GCMs compared in this study have a general tendency

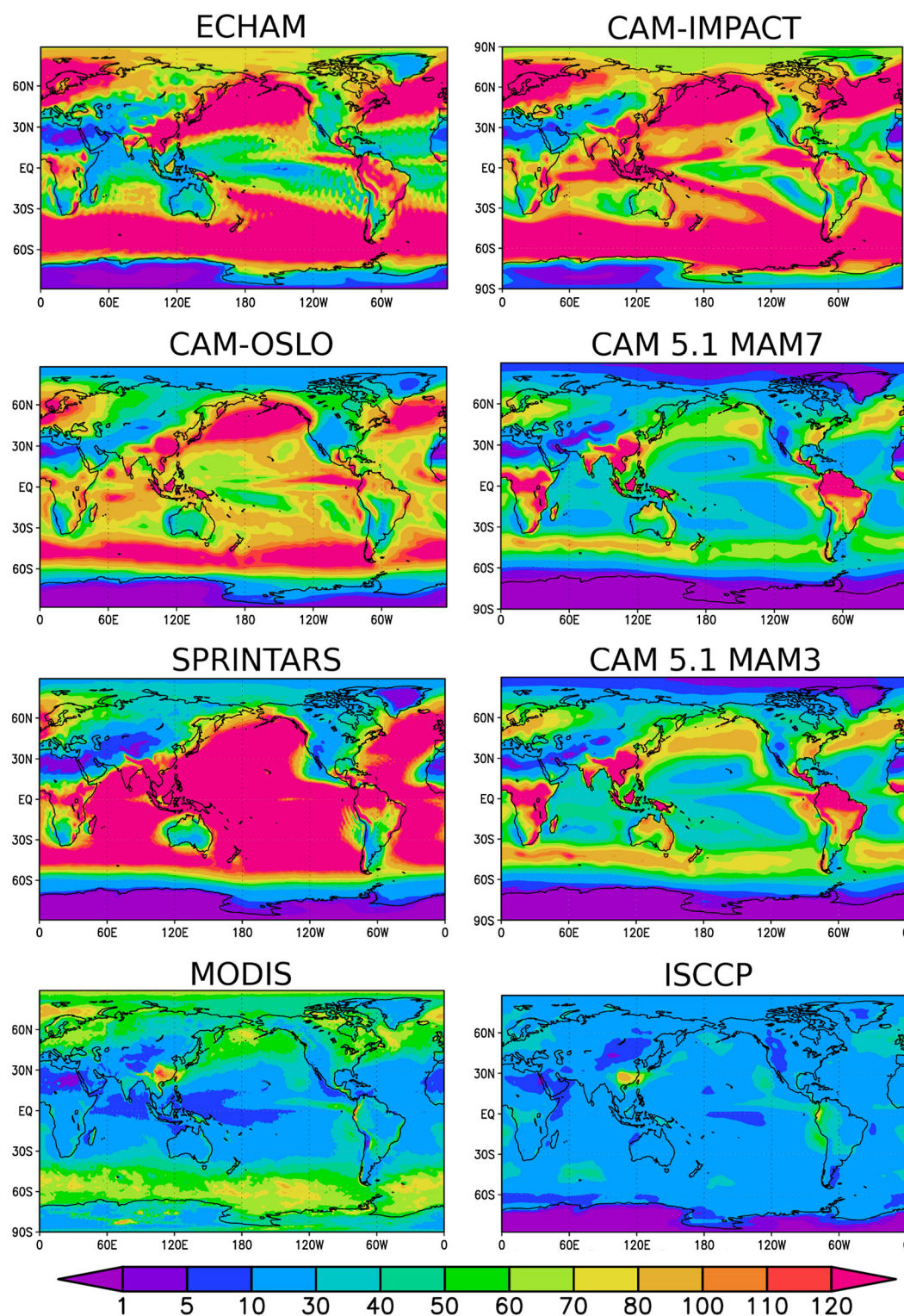


Figure 1. LWP (g m^{-2}) as simulated by the six GCMs and observed by ISCCP and MODIS.

to overestimate the LWP (particularly over the oceans) and underestimate the IWP compared to observations provided through satellite retrievals. While CAM5.1 produces similar spatial structures of LWP and IWP with both the three- and seven-mode aerosol schemes, the LWP is consistently larger over the oceans for the three-mode scheme. The larger LWP of MAM3 is due to the larger concentrations of sea salt obtained in

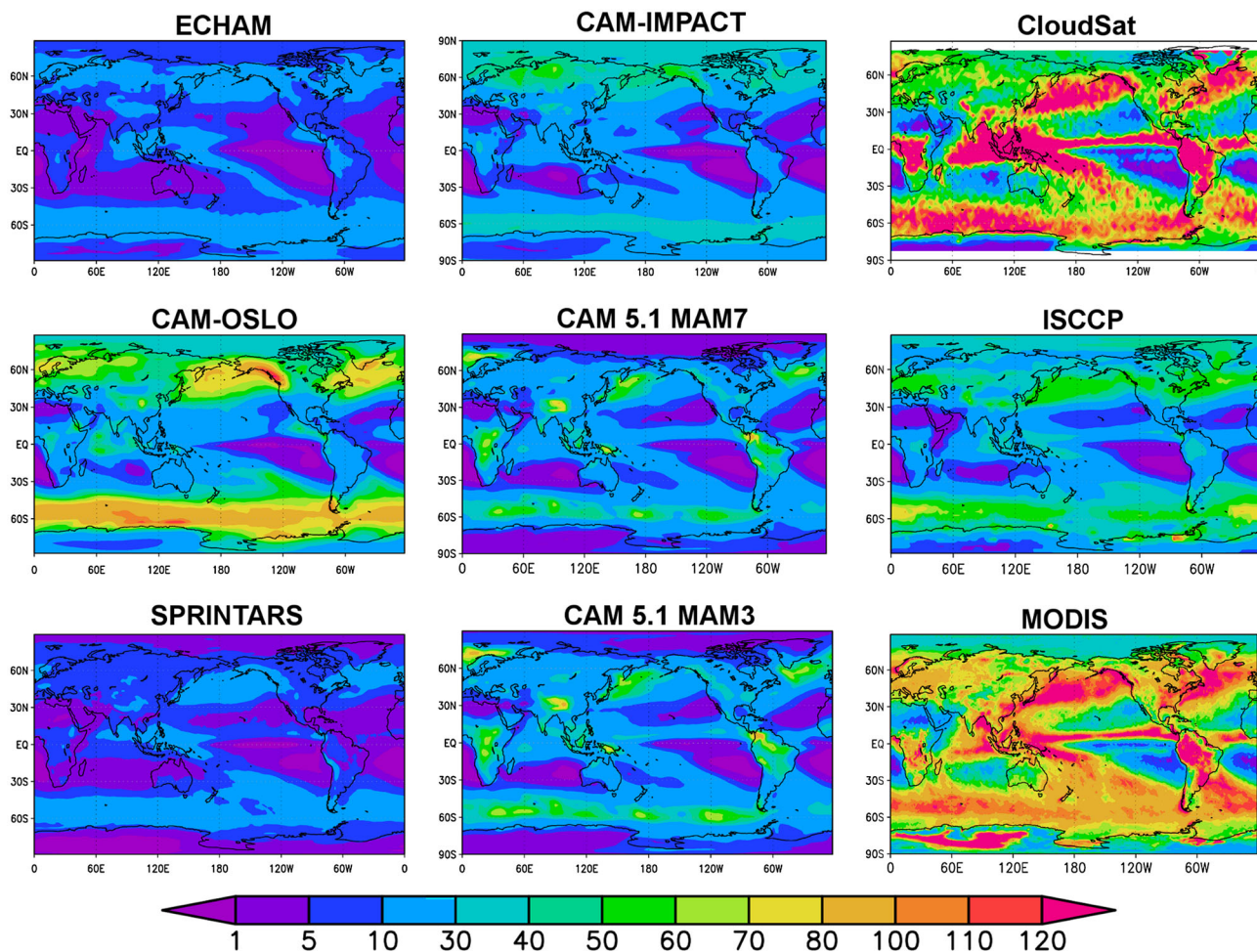


Figure 2. IWP (g m^{-2}) as modeled by the six GCMs and observed by CloudSat, ISCCP, and MODIS.

MAM3 compared to MAM7, which increase the LWP through aerosol-cloud interactions [Liu *et al.*, 2012]. ECHAM6 and CAM-IMPACT have similar global spatial distributions of LWP except around the equator, where the latter model retains more liquid water. Despite the relatively similar distributions of LWP of ECHAM6 and CAM-IMPACT, the magnitudes of IWP they predict are different, with CAM-IMPACT producing more ice overall. SPRINTARS produces a large land-sea contrast in LWP, which is not supported by the satellite observations. CAM-Oslo produces the largest IWP while producing also a relatively large LWP. While all models significantly underestimate the observed IWP, the IWP produced by CAM-Oslo is the closest in magnitude. One reason for the larger IWP for MODIS and CloudSat compared to the GCMs and ISCCP is that CloudSat includes the precipitating ice particles when calculating the IWP. ISCCP is sensitive to small particle sizes; therefore, it only includes suspended ice (liquid) particles in IWP (LWP). The models used in the MODIS retrievals do not contain precipitation; they assume particle size distributions consistent with suspended liquid or ice. Sometimes, the clouds observed by MODIS can contain precipitation [e.g., Lebsock *et al.*, 2011]. Precipitation tends to increase the retrieved particle size; the amount of this increase depends on the precipitation amount, location, and other factors. GCMs, on the other hand, do not include precipitating hydrometeors in LWP or IWP calculations. When precipitating ice particles are excluded from CloudSat as in Jiang *et al.* [2012], the observed IWP is comparable to ISCCP.

Table 3 summarizes the globally averaged values of annual mean 2-D fields for all GCMs and their standard deviation. The largest LWP and smallest IWP are obtained with SPRINTARS. While CAM5.1 (with both MAM3 and MAM7) and CAM-IMPACT produce similar global mean values of IWP, the global mean LWP produced by the latter GCM is twice as large as that produced by the former. CAM-Oslo produces the largest global mean

Table 3. Global Annual Mean Properties Obtained From Multiyear Means From Six GCMs for Two Experiments and Standard Deviations of the Individual Annual Mean Fields From the Multiyear Means for Six GCMs^a

GCMs	LWP (g m^{-2})	IWP (g m^{-2})	TWP (g m^{-2})	LWCF (W m^{-2})	SWCF (W m^{-2})	CLD (%)	FSNS (W m^{-2})	FSNT (W m^{-2})	FLNS (W m^{-2})	FLNT (W m^{-2})	ICNUM ($\times 10^8 \text{ m}^{-2}$)	CDNUM ($\times 10^{10} \text{ m}^{-2}$)
<i>Experiment 1</i>												
ECHAM6	86.27 \pm 0.31	7.71 \pm 0.01	93.98 \pm 0.3	27.09 \pm 0.08	-53.07 \pm 0.1	62.35 \pm 0.11	160.28 \pm 0.14	235.02 \pm 0.1	53.71 \pm 0.17	234.49 \pm 0.09	16.6 \pm 0.08	3.77 \pm 0.01
CAM-IMPACT	98.74 \pm 0.41	17.13 \pm 0.05	115.87 \pm 0.4	31.48 \pm 0.08	-58.83 \pm 0.22	66.55 \pm 0.09	156.55 \pm 0.25	230.37 \pm 0.21	53.8 \pm 0.15	229.33 \pm 0.28	12.2 \pm 0.94	3.43 \pm 0.01
CAM-OSLO	75.27 \pm 0.51	33.89 \pm 0.21	109.16 \pm 0.64	29.45 \pm 0.08	-57.68 \pm 0.28	62.48 \pm 0.13	155.92 \pm 0.31	231.89 \pm 0.27	55.39 \pm 0.18	233.22 \pm 0.08	27.9 \pm 0.08	2.89 \pm 0.01
CAM5.1 MAM7	44.53 \pm 0.2	17.72 \pm 0.13	62.25 \pm 0.26	24.08 \pm 0.11	-51.98 \pm 0.17	64.09 \pm 0.21	160.47 \pm 0.26	236.05 \pm 0.21	53.42 \pm 0.17	233.74 \pm 0.19	0.93 \pm 0.009	1.29 \pm 0.02
CAM5.1 MAM3	52.33 \pm 0.34	18.84 \pm 0.05	71.17 \pm 0.38	25.4 \pm 0.06	-54.44 \pm 0.21	65.65 \pm 0.14	156.91 \pm 0.24	236.32 \pm 0.2	51.16 \pm 0.17	232.14 \pm 0.08	1.01 \pm 0.004	1.72 \pm 0.01
SPRINTARS	108.97 \pm 0.71	7.04 \pm 0.3	116.01 \pm 0.91	27.12 \pm 0.5	-53.02 \pm 0.2	72.96 \pm 0.2	157.96 \pm 0.28	234.09 \pm 0.2	56.49 \pm 0.19	237.04 \pm 0.34	49.8 \pm 1.7	14.2 \pm 0.003
GCM Mean	77.685	17.055	94.74	27.44	-54.84	65.68	158.02	233.96	54.00	233.33	18.09	4.57
<i>Experiment 2</i>												
ECHAM6	88.8 \pm 0.74	7.62 \pm 0.04	96.42 \pm 0.67	27.46 \pm 0.16	-53.51 \pm 0.27	62.54 \pm 0.12	159.77 \pm 0.33	234.43 \pm 0.32	53.61 \pm 0.15	233.97 \pm 0.18	16.6 \pm 0.09	3.82 \pm 0.04
CAM-IMPACT	107.09 \pm 0.64	15.47 \pm 0.09	122.56 \pm 0.69	32.71 \pm 0.05	-61.31 \pm 0.14	66.93 \pm 0.1	154.39 \pm 0.23	227.79 \pm 0.23	53.22 \pm 0.07	228.05 \pm 0.37	12.6 \pm 0.84	3.92 \pm 0.007
CAM-OSLO	108.85 \pm 0.31	20.66 \pm 0.07	129.51 \pm 0.33	30.75 \pm 0.04	-60.88 \pm 0.12	63.58 \pm 0.2	153.27 \pm 0.17	227.78 \pm 0.18	55.67 \pm 0.04	231.68 \pm 0.04	12.2 \pm 0.03	2.26 \pm 0.01
CAM5.1 MAM7	46.26 \pm 0.18	16.06 \pm 0.06	62.32 \pm 0.16	23.69 \pm 0.09	-52.04 \pm 0.1	64.01 \pm 0.13	160.31 \pm 0.22	235.99 \pm 0.19	53.1 \pm 0.09	233.78 \pm 0.18	0.88 \pm 0.002	1.42 \pm 0.01
CAM5.1 MAM3	55.3 \pm 0.37	17.21 \pm 0.13	72.51 \pm 0.37	25.74 \pm 0.1	-55.26 \pm 0.21	65.81 \pm 0.09	156.06 \pm 0.2	235.57 \pm 0.19	50.58 \pm 0.08	231.64 \pm 0.14	0.98 \pm 0.008	1.9 \pm 0.02
SPRINTARS	107.45 \pm 0.45	6.74 \pm 0.2	114.19 \pm 0.6	26.58 \pm 0.33	-52.35 \pm 0.23	72.76 \pm 0.15	158.67 \pm 0.27	234.69 \pm 0.21	56.76 \pm 0.19	237.48 \pm 0.14	42.8 \pm 0.77	14.2 \pm 0.006
GCM Mean	85.625	13.96	99.585	27.82	-55.89	65.94	157.08	232.71	53.82	232.77	14.36	4.59
OBSERVED	20–33	27–76	47–109	26–30	-45 to -51	67	162–171	226–237	51–71	233–254	-	4

^aProperties listed are liquid water path (LWP), ice water path (IWP), total water path (TWP), longwave cloud radiative forcing (LWCF), shortwave cloud radiative forcing (SWCF), total cloud fraction (CLD), net shortwave flux at the surface (FSNS), net shortwave flux at the top of the atmosphere (FSNT), net longwave flux at the surface (FLNS), net longwave flux at the top of the atmosphere (FLNT), vertically integrated ice crystal number concentration (ICNUM), and cloud droplet number concentration (CDNUM). Observations of LWP are taken from MODIS and ISCCP. Observational range of IWP is obtained from MODIS, ISCCP, and CloudSat, while CLD is from ISCCP. LWCF and SWCF range are obtained from Loeb *et al.* [2009]; FLNS, FLNT, and FSNT are from Trenberth *et al.* [2009] and FSNS is from Stephens *et al.* [2012] using various satellite observations. Observed CDNUM is from Han *et al.* [1998].

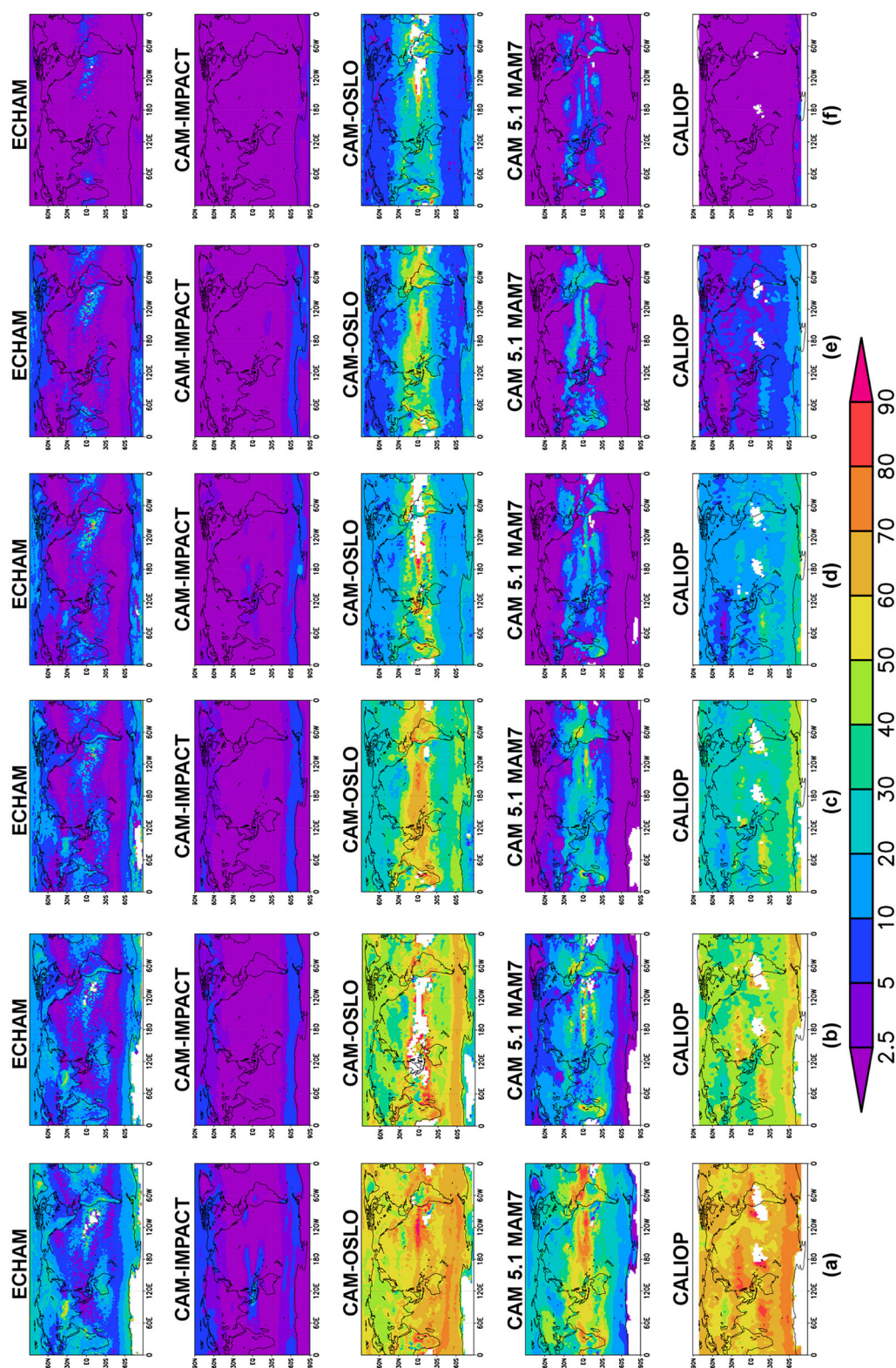


Figure 3. Global maps of annual mean SLF (%) on isotherms (a) — 10°C, (b) — 15°C, (c) — 20°C, (d) — 25°C, (e) — 30°C, and (f) — 35°C for four GCMs and CALIOP observations for Experiment 1.

IWP while retaining a relatively high global mean LWP compared to the other GCMs. All GCMs produce radiative fluxes and cloud radiative forcing within or close to (\sim roughly 15%) the range of observations (Table 3). Although all GCMs overpredict the LWP compared to observations, all models, except SPRINTARS (which has the highest LWP), underestimate the vertically integrated number of cloud droplets (Table 3). The vertically integrated cloud droplet concentration is calculated by adding the droplet number concentrations (averaged over all-sky conditions) in each grid box from the surface to the top of the atmosphere. The two models with next highest LWP (ECHAM6 and CAM-IMPACT) are within 6% and 15% of the observed number concentration, respectively. The global annual mean vertically integrated number of ice crystals in the models amounts roughly to between 1 and 10% of the vertically integrated number of cloud droplets of each model (Table 3). In Table 3, in addition to heterogeneously formed ice crystals, the vertically integrated ice crystal number concentration includes ice crystals formed homogeneously below -40°C .

To illustrate the differences in the phase partitioning of cloud water, we calculate the SLF for four of the GCMs and observations as explained in the section 3 (the remaining two models did not report SLF). Figure 3 shows the global distribution of SLF on six isotherms (-10 , -15 , -20 , -25 , -30 , and -35°C) for the GCMs and for CALIOP-based observations. As the temperature decreases, the spatial structure of the remaining supercooled liquid water in clouds differs among the GCMs. The maximum of supercooled liquid water resides around the poles in both hemispheres for CAM-IMPACT, while for CAM5.1 MAM7 and CAM-Oslo the maximum in SLF is located around the equator. For ECHAM6, two maxima are present with one around the poles and another one around the equator. The observed SLF goes through a steady and gradual reduction toward colder temperatures from a global annual mean value of 64% at -10°C to less than 1% at -35°C . The models do not reproduce this distinctive pattern. In general, the simulated SLFs are too low at warm temperatures and too high at low temperatures. While the observed magnitude of the SLF is captured by CAM-Oslo for warm temperatures, none of the models are fully capable of reproducing the spatial distribution and magnitude of the observed SLF at any isotherms. For most models, some supercooled liquid water remains at -35°C , while the observed SLF has only a small fraction of supercooled liquid water left around 70 – 80°S , which seems to be best captured with CAM-IMPACT.

Zonal mean SLFs calculated at six isotherms for GCMs and CALIOP-based observations are given in Figure 4a. Even though CAM-Oslo produces the highest SLF among the four GCMs and is more similar to observations at warmer temperatures ($T > -25^{\circ}\text{C}$), it overestimates the SLF at colder temperatures. Aside from CAM-Oslo, CAM5.1 MAM7 also produces a higher SLF compared to the other two GCMs and is in better agreement with the observations, although the simulated peak in the tropics appears not to be realistic. CAM-IMPACT and ECHAM6 both underestimate the SLF at warmer temperatures ($T > -25^{\circ}\text{C}$), while at colder temperatures they provide a better match to observations.

Interestingly, despite the larger magnitude of the CAM-IMPACT- and ECHAM6-simulated LWP, the amount of liquid water at temperatures that allow for mixed-phase clouds is smallest for these two models. More liquid water remains in both CAM-Oslo and CAM5.1 MAM7 at mixed-phase cloud temperatures, despite the relatively smaller magnitude of simulated LWP of the latter GCM. This result underscores the importance of validating models with observations that provide information not only on the total integrated amount of liquid and ice but also their vertical distributions. On a side note, when calculating the SLF from CALIOP observations, if horizontally oriented ice crystals are ignored, the observed SLF increases ($\sim 20\%$ at -10°C) and the latitudinal change in the zonal mean SLF is reduced [Komurcu *et al.*, 2013]. Horizontally oriented ice crystals occur more often at temperatures between 0 and -20°C with certain ice crystal habits and when the cloud circulations are weak [Hu *et al.*, 2009]. Therefore, to validate and constrain the parameterization of mixed-phase cloud processes in GCMs, it is important that satellite retrievals identify the cloud water phase accurately.

We now look into the annual and zonal mean vertical profiles to investigate the differences among the GCMs. Figure 5a shows the annual mean and zonally averaged profiles of potential IN concentrations obtained from six GCMs. In our study, potential IN are defined as the number concentration of particles that can act as IN. For each GCM, the species contributing to potential IN are different and depend on the GCM specific aerosol schemes and how each GCM characterizes the aerosols as IN and non-IN. Potential IN are dust and BC aerosols for ECHAM6, CAM-Oslo, and SPRINTARS; dust, BC, and OM for CAM-IMPACT; and dust aerosols for CAM5.1 MAM3 and MAM7. The number of particles that can act as IN is quite different both in magnitude and vertical distributions among the six GCMs (Figure 5a) except for CAM5.1 MAM3 and MAM7. MAM7 has slightly

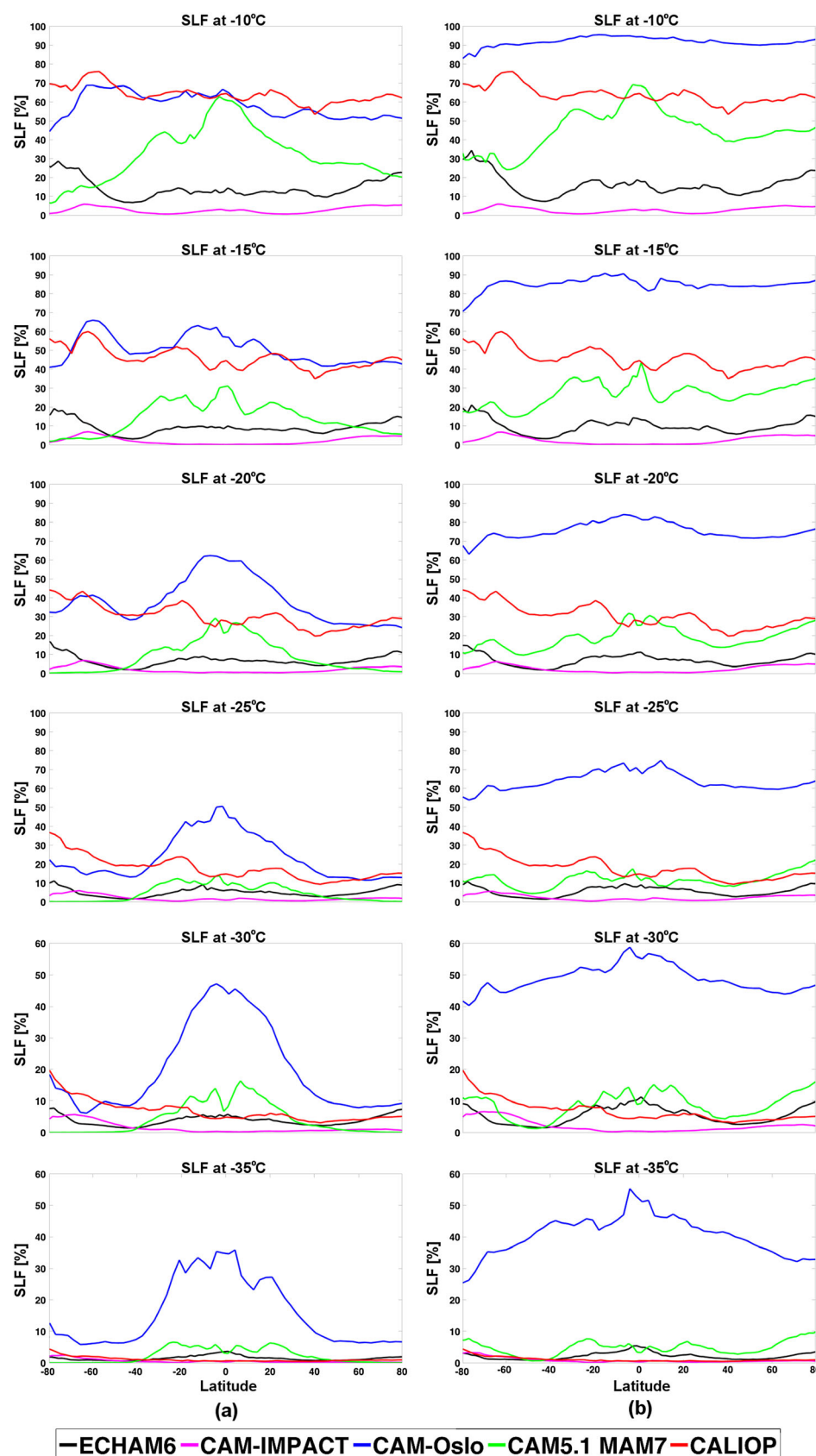


Figure 4. Zonal Mean SLF (%) at six isotherms for four GCMs and CALIOP observations for (a) Experiment 1 and (b) Experiment 2.

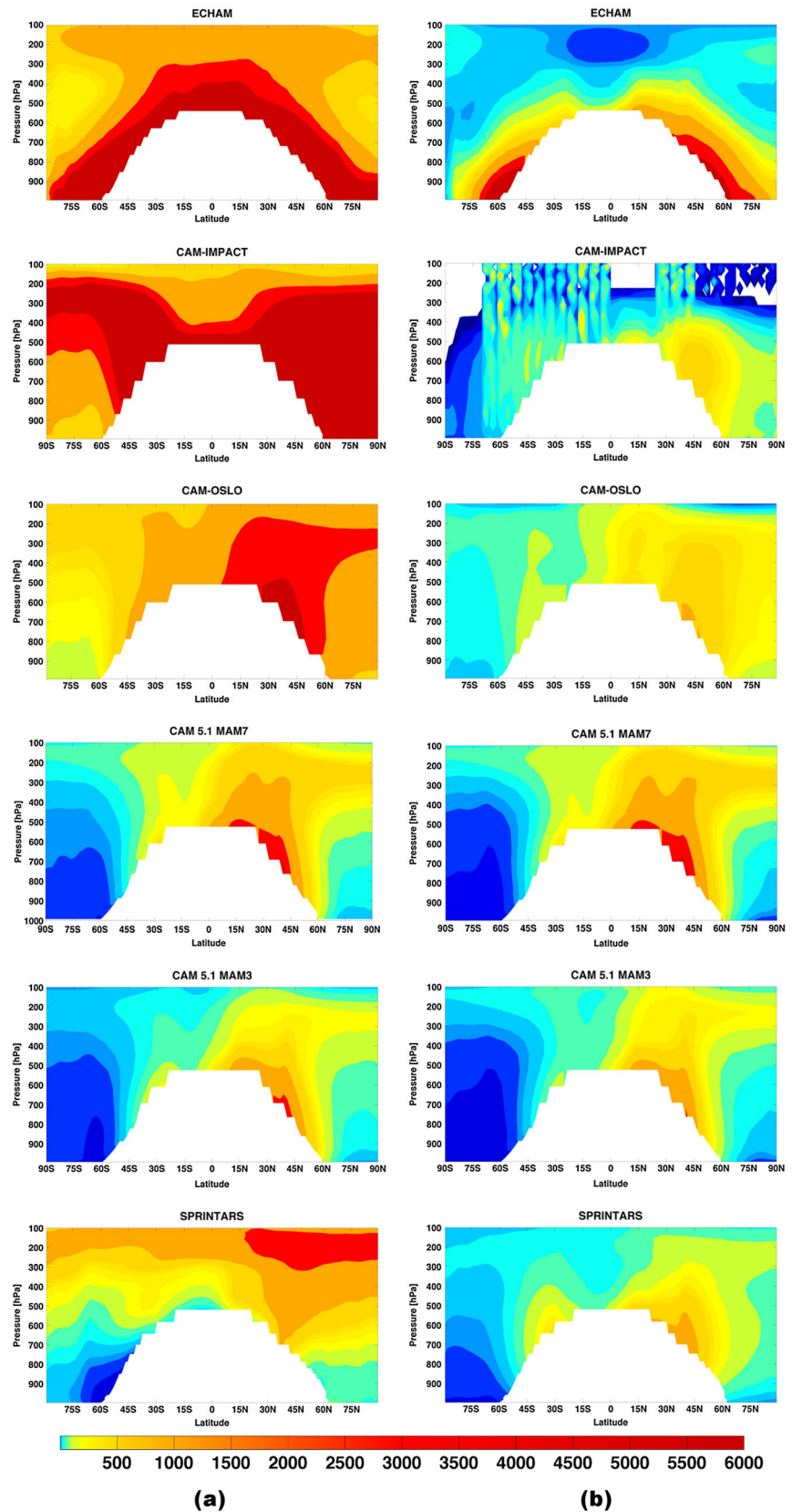


Figure 5. Zonal mean profiles of annual mean (a) potential IN in Experiment 1 (L^{-1}) and (b) potential IN larger than $0.5 \mu m$ in Experiment 2 (L^{-1}).

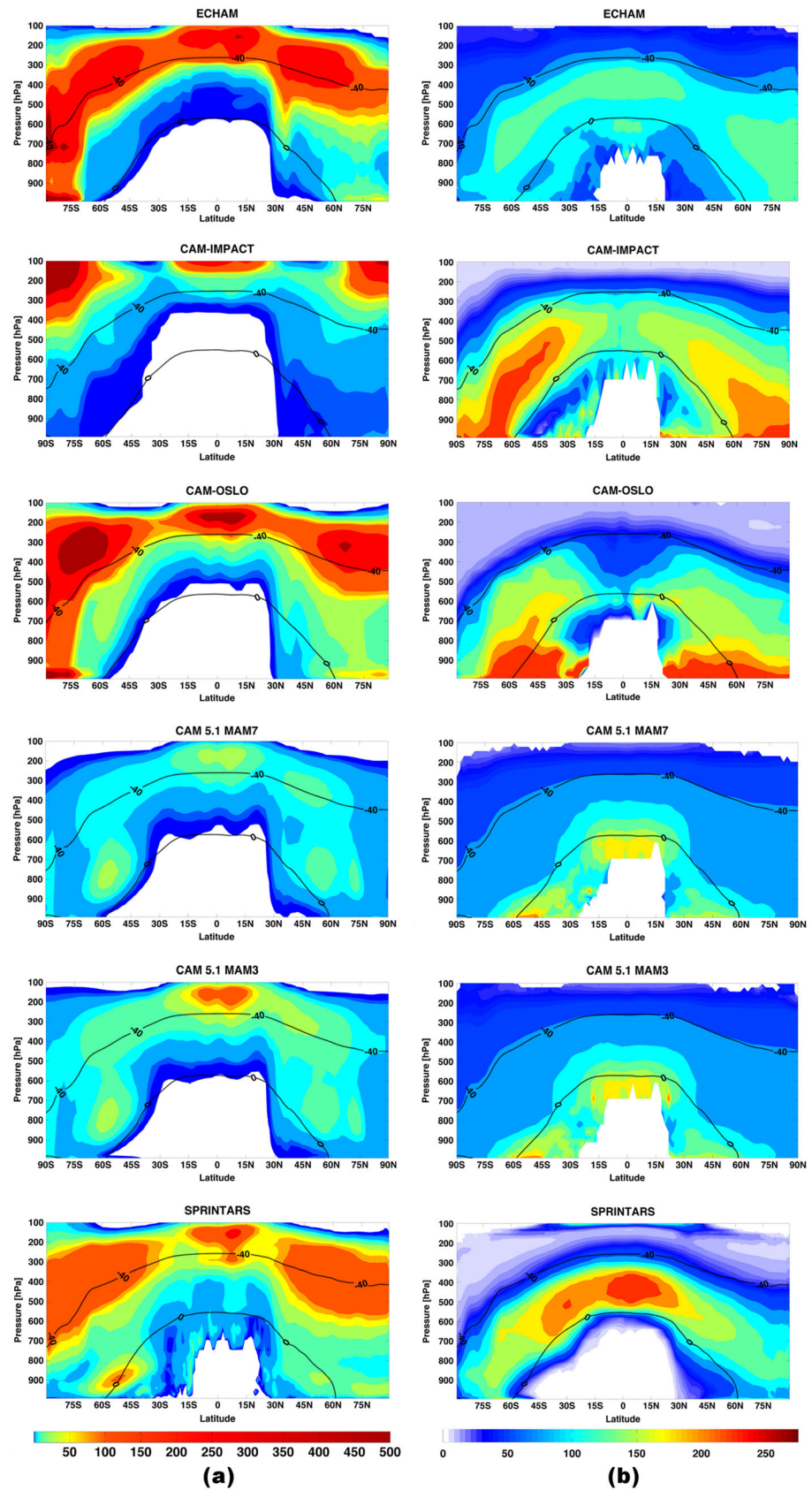


Figure 6

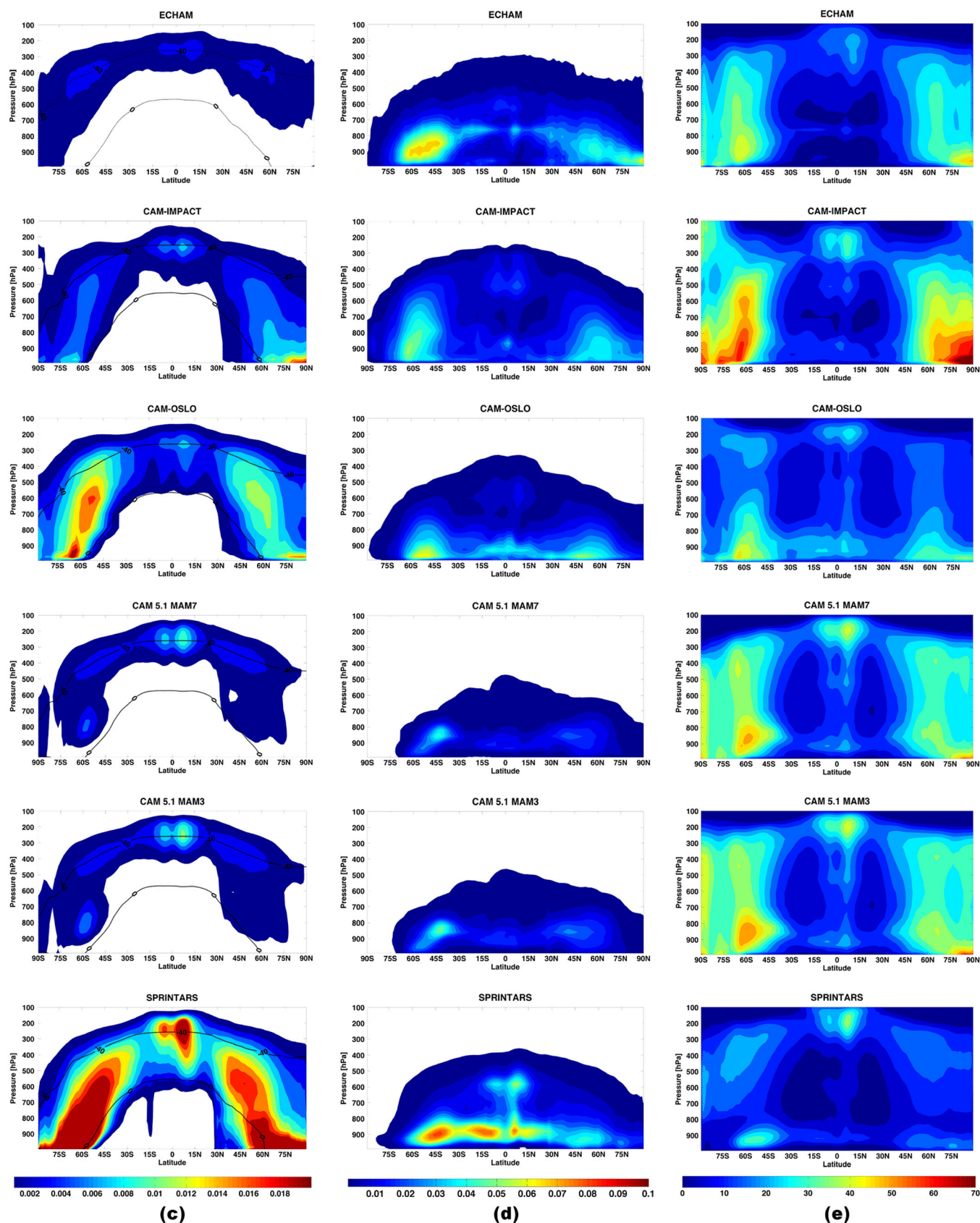


Figure 6. (continued)

larger potential IN compared to MAM3 as expected due to the different cutoff size ranges and standard deviations of lognormal size distributions along with differences in the mixing states assumed in the three- and seven-mode aerosol schemes [Liu *et al.*, 2012]. Despite the same aerosol species used as potential IN for CAM-Oslo, ECHAM6, and SPRINTARS, the large differences in the vertical distribution and magnitude of the aerosols are striking. Figure 6 shows the annual mean and zonally averaged profiles of grid box mean ice crystal concentrations (Figure 6a), ice crystal effective radius (Figure 6b), grid box mean ice mass mixing ratio (Figure 6c), grid box mean liquid water mass mixing ratio (Figure 6d), and cloud fraction (Figure 6e) for Experiment 1. It is important to emphasize that while our aim is to investigate the differences in the models' phase partitioning of cloud water in mixed-phase clouds, the results presented in Figure 6 are not solely representative of mixed-phase clouds. With the profiles, we aim to provide the differences in the properties of ice-containing clouds in GCMs, but in the discussion below, the emphasis will be on the properties of clouds that occupy the temperature range relevant for mixed-phase clouds. There are significant differences in the simulated IN and ice crystal concentrations among the models [Figures 5a and 6a]. CAM5.1 (with both MAM3 and MAM7) produces lower ice crystal concentrations compared to the other GCMs (except CAM-IMPACT). There are more ice crystals in MAM3 compared to MAM7 in the upper troposphere because the larger number of dust IN in MAM7 reduces the efficiency of homogeneous ice nucleation. Despite simulating high IN concentrations (Figure 5a), CAM-IMPACT produces relatively few (Figure 6a) and large ice crystals (Figure 6b). On the contrary, SPRINTARS produces high ice crystal concentrations at mixed-phase cloud temperatures (Figure 6a) and the highest vertically integrated ice crystal concentration (Table 3) despite its relatively low IN concentrations (Figure 5a). As evident from Figure 5a, for mixed-phase clouds, the concentrations of aerosol particles that may act as IN alone are not good predictors of ice crystal concentrations, which also depend on the ice nucleation parameterization and subsequent ice crystal sources and sinks. In the upper atmosphere, at temperatures below -40°C , the difference between the number of ice crystals and IN can be explained through the homogeneous ice nucleation of sulfate aerosols making the IN concentrations in Figure 5a irrelevant.

Once ice crystals are nucleated, their subsequent growth and sedimentation determine the cloud water mass mixing ratios and the sizes of the crystals. ECHAM6, CAM-Oslo, and SPRINTARS produce similar profiles of ice crystal number concentrations in mixed-phase cloud regions with different magnitudes (Figure 6a). Despite this similarity, the three GCMs produce quite different vertical profiles of ice crystal effective radius with the largest crystal sizes concentrating below 700 hPa for CAM-Oslo and above 700 hPa for ECHAM6 and SPRINTARS (Figure 6b). In addition, the largest ice crystal sizes are about a factor of 2 smaller for ECHAM6 compared to SPRINTARS and CAM-Oslo (Figure 6b). Similarly, the profile of mass mixing ratio of ice is also different among the three GCMs (Figure 6c). Furthermore, the fewer ice crystals in CAM-IMPACT lead to the largest ice crystals among all GCMs in mixed-phase cloud regions, while SPRINTARS produces particularly large crystals in tropics (Figure 6d). The differences in model-simulated ice effective radius and mass despite the similar ice crystal number concentrations point out the importance of the ice crystal growth and precipitation processes of the GCMs on simulated cloud microphysical quantities.

Due to the fewer and larger ice crystals in CAM-IMPACT, less liquid water mass is consumed in the growth of ice crystals (WBF process); therefore, the model also produces a large liquid water mass with a large vertical and horizontal extent (Figure 6d). As a result, there are more low-level clouds in CAM-IMPACT compared to all other GCMs (Figure 6e). The vertical distribution of annual mean cloud fraction is quite similar among the GCMs while the magnitude differs (Figure 6e). Finally, despite the lesser horizontal and vertical extents and magnitude of the liquid water mass in CAM5.1 (Figure 6d), the fractional amount of supercooled liquid water remaining in the cloud is larger at all isotherms compared to the other GCMs (except CAM-Oslo) and is relatively more in line with the observations of SLF (Figures 3 and 4). Based on the results of this section, we can conclude that model-simulated differences in phase partitioning depend not only on the differences in ice nucleation parameterization but also on other parameterized cloud ice processes subsequent to the nucleation of ice crystals such as ice crystal growth and precipitation. To understand the relative importance

Figure 6. Zonal mean profiles of annual mean in (a) ice crystal number concentration (L^{-1}) and (b) ice effective radius (μm), (c) cloud ice mass mixing ratio (g/kg), (d) cloud liquid water mass mixing ratio (g/kg), and (e) cloud fraction (%) for all models. In a, b and c isotherms of 0 and -40°C are plotted to indicate the regions where mixed-phase clouds can occur.

Table 4. Difference in Global Annual Fields Obtained From Multiyear Means Between the Two Experiments (Experiment 2 – Experiment 1) and Standard Deviations of the Individual Annual Mean Fields From the Multiyear Means for Six GCMs

GCMs	LWP (g m^{-2})	IWP (g m^{-2})	LWCF (W m^{-2})	SWCF (W m^{-2})	CLD (%)	FSNS (W m^{-2})	FSNT (W m^{-2})	FLNS (W m^{-2})	FLNT (W m^{-2})	ICNUM (m^{-2})	CDNUM (m^{-2})
ECHAM6	2.53 \pm 0.6	-0.09 \pm 0.04	0.37 \pm 0.12	-0.44 \pm 0.17	0.19 \pm 0.09	-0.51 \pm 0.22	-0.59 \pm 0.21	-0.1 \pm 0.21	-0.52 \pm 0.19	-0.002 \pm 0.15 $\times 10^8$	0.05 \pm 0.03 $\times 10^{10}$
CAM-IMPACT	8.35 \pm 0.44	-1.66 \pm 0.11	1.23 \pm 0.09	-2.48 \pm 0.19	0.38 \pm 0.14	-2.16 \pm 0.3	-2.58 \pm 0.25	-0.58 \pm 0.17	-1.28 \pm 0.14	0.45 \pm 0.48 $\times 10^8$	0.49 \pm 0.01 $\times 10^{10}$
CAM-OSLO	33.58 \pm 0.8	-13.23 \pm 0.27	1.3 \pm 0.11	-3.21 \pm 0.37	1.1 \pm 0.3	-2.65 \pm 0.45	-4.11 \pm 0.42	0.28 \pm 0.22	-1.54 \pm 0.07	-15.7 \pm 0.07 $\times 10^8$	-0.63 \pm 0.02 $\times 10^{10}$
CAM5.1 MAM7	1.73 \pm 0.25	-1.66 \pm 0.18	-0.39 \pm 0.10	-0.06 \pm 0.2	-0.08 \pm 0.16	-0.16 \pm 0.27	-0.06 \pm 0.25	-0.32 \pm 0.15	0.04 \pm 0.22	-0.05 \pm 0.008 $\times 10^8$	0.13 \pm 0.03 $\times 10^{10}$
CAM5.1 MAM3	2.97 \pm 0.53	-1.63 \pm 0.10	0.34 \pm 0.13	-0.82 \pm 0.35	0.16 \pm 0.17	-0.85 \pm 0.34	-0.75 \pm 0.31	-0.58 \pm 0.19	-0.5 \pm 0.17	-0.03 \pm 0.007 $\times 10^8$	0.18 \pm 0.02 $\times 10^{10}$
SPRINTARS	-1.52 \pm 0.87	-0.3 \pm 0.23	-0.54 \pm 0.35	0.67 \pm 0.33	-0.2 \pm 0.31	0.71 \pm 0.51	0.6 \pm 0.37	0.27 \pm 0.33	0.44 \pm 0.49	-7 \pm 1.26 $\times 10^8$	-0.06 \pm 0.04 $\times 10^{10}$

of ice nucleation parameterization on cloud phase partitioning among cloud ice processes, we perform a new set of experiments in the next section.

4.2. Impacts of Ice Nucleation

In this section, we explore the importance of ice nucleation parameterizations in creating differences in the GCM-simulated cloud water phase relative to the parameterizations of other processes that can influence phase partitioning such as ice crystal growth and sedimentation. We analyze the influence of ice nucleation parameterization on model-simulated fields by using a fixed ice nucleation mechanism that replaces the default ice nucleation parameterizations of the GCMs for mixed-phase clouds as explained in section 3. With Experiment 2, we seek answers to the following questions: How sensitive are the modeled fields of IWP, LWP, and SLF to the choice of ice nucleation parameterization? Will a fixed ice nucleation scheme reduce intermodel spread in these simulated fields? The differences in GCM-simulated cloud water phase can be a result of many factors, including the differences in the large-scale and convective cloud parameterizations of the models. When the experiments were conducted, we had no prior expectation about how the alternative parameterization would affect each individual model, but the differences in simulated phase partitioning or water contents were not expected to completely disappear with a fixed ice nucleation parameterization. However, because of the importance of ice nucleation in phase partitioning as described in sections 1 and 3, we expected the fixed ice nucleation parameterization to reduce the spread of the models to some extent. It is well known that microphysics influence water contents in both cloud resolving and global climate models: For example, cloud water contents and other cloud properties change with changes in autoconversion rates or changes in ice nucleation parameterizations in GCMs [e.g., Gettelman *et al.*, 2010; DeMott *et al.*, 2010; Yun and Penner, 2013; Xie *et al.*, 2013]. Furthermore, four of the models used in this study are CAM derivatives with many other model components in common, which makes it rational to presume differences due to different microphysics parameterizations. Hence, we are simply using Experiment 2 to deduce the sensitivity of the GCM-simulated cloud water phase to ice nucleation relative to other cloud ice processes.

With the implementation of the fixed ice nucleation mechanism, total water path (TWP) and the LWP increase for all GCMs except for SPRINTARS, while the IWP decreases for all GCMs (Tables 3 and 4). The TWP increases in all GCMs (except for SPRINTARS) as a result of the dominance of the increase in the LWP as opposed to the reduction in the IWP. Because IN concentrations are restricted only to the model-predicted concentrations of insoluble particles larger than 0.5 μm in the DeMott *et al.* [2010] parameterization, introducing it tends to reduce the number of IN for all GCMs. As a consequence, ice crystal concentrations and the conversion of liquid to ice through the WBF process are reduced, hence the reduction in IWP and increase in LWP seen in most models. Both CAM-OSLO and CAM-IMPACT produce a significant increase in TWP in Experiment 2 compared to Experiment 1 (Table 3). The positive change in TWP is smallest for CAM5.1 MAM7 and CAM5.1 MAM3, both of which produce only modest increases in TWP (Table 3). Table 4 summarizes the global and annual averages of the differences in the annual mean 2-D fields for all

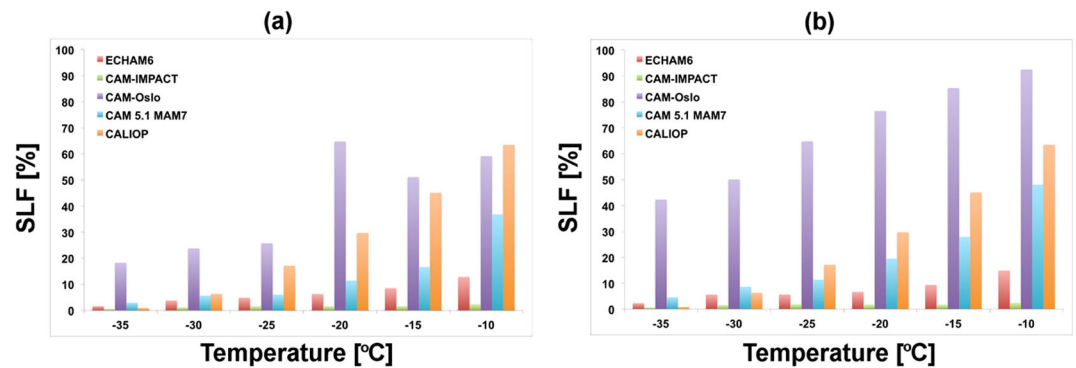


Figure 7. Global annual mean SLF (%) obtained from GCMs at six isotherms for (a) Experiment 1 and (b) Experiment 2 along with SLF (%) from CALIOP observations.

GCMs. The differences presented in Table 4 are generally statistically significant. Because of the uncertainties associated with the satellite retrievals, the observed values have relatively large uncertainties associated with them, which in some cases can be larger than the sensitivity of model results to the ice nucleation. For MAM7, the increase in LWP is almost entirely balanced by the reduction in IWP (Table 4).

Figure 4b shows the zonally averaged annual mean SLF for all models at six isotherms along with the data based on the CALIOP observations. With the same ice nucleation mechanism, all GCMs produce a higher SLF compared to Experiment 1. CAM-Oslo produces the largest increase in SLF and overestimates the SLF compared to observations at all isotherms. All other GCMs still underestimate the SLF relative to CALIOP for $T > -30^{\circ}\text{C}$, CAM5.1 MAM7 less so than ECHAM6 and SPRINTARS. While CAM-IMPACT and ECHAM6 also result in an increased SLF in Experiment 2, the increase in SLF is small compared to CAM-Oslo and CAM5.1. The partitioning of cloud water as implied by the SLF changes considerably between the two experiments for CAM5.1-MAM7, while there is a relatively small change in the TWP for the same model compared to other GCMs.

To show the extent of the spread in the model-predicted SLF, global annual mean SLFs from all GCMs at six isotherms are plotted in Figure 7 for both experiments along with CALIOP observations. Despite the implementation of the same ice nucleation mechanism in Experiment 2, the spread in the simulated SLF among the GCMs is not reduced (Figure 7). As in Experiment 1, neither of the models is fully capable of capturing the spatial distribution and magnitude of the observed SLF in Experiment 2 (Figures 4 and 7). Although with the *DeMott et al.* [2010] nucleation, the phase partitioning between cloud liquid water and ice is improved for most models; it is not necessarily a better ice nucleation parameterization: The LWP (IWP), which is already overestimated (underestimated) with respect to observations, increases (decreases) for most models (Table 4).

To further illustrate the higher global values of SLF obtained with the implementation of the fixed ice nucleation, we present the normal distribution fit to the probability density function (PDF) of the global distribution of annual mean SLF for the GCMs and observations at six isotherms for both experiments in Figure 8. The distributions of SLF are different for all GCMs at all isotherms in both experiments, and none of the PDFs of the models match the observed distributions. ECHAM6 simulates realistic variability in SLF for a given isotherm, as illustrated by the widths of the PDFs, but the PDFs are shifted toward too low values. CAM-IMPACT also exhibits this shift and underestimates the variability. CAM-Oslo simulates realistic widths for warm temperatures ($T > -25^{\circ}\text{C}$), but the PDFs are too wide for the lowest temperatures. CAM5.1 MAM7 compares relatively well with observations for the coldest isotherms, while the PDFs for the warmest isotherms are too wide and shifted toward lower SLFs compared to CALIOP. For Experiment 2, with the fixed ice nucleation, the distribution of SLF shifts toward larger SLF values for all GCMs. These shifts are the largest for CAM-Oslo followed by CAM5.1, while the shifts are subtle for ECHAM6 and only minor for CAM-IMPACT. While CAM-Oslo is sensitive to ice nucleation in terms of significant changes in both water paths and in the SLF, CAM5.1 MAM7 seems to be sensitive in terms of SLF only. The changes in the downwelling solar radiation at the surface for these two most sensitive GCMs between Experiment 1 (GCMs default heterogeneous ice nucleation) and Experiment 2 (ice nucleation following *DeMott et al.* [2010]) are -3 W m^{-2} for CAM-Oslo and

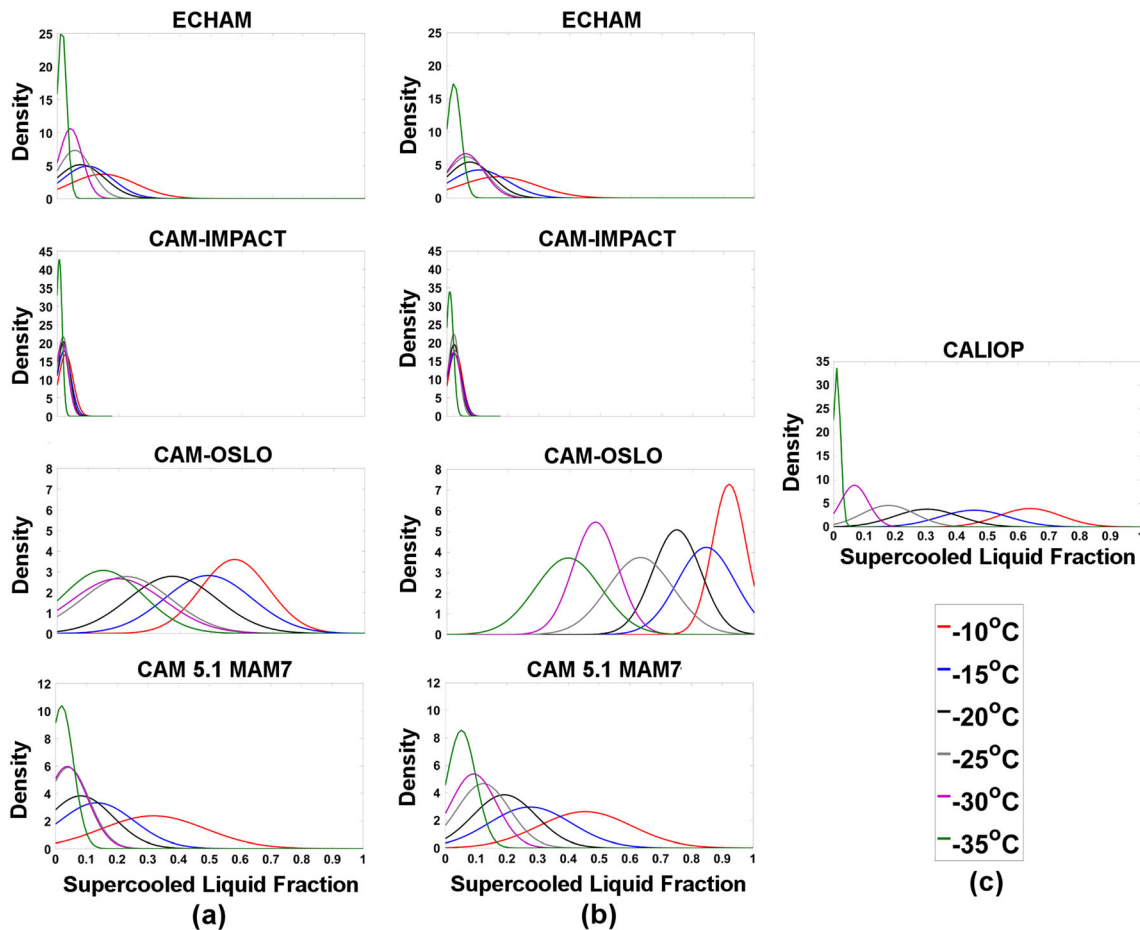


Figure 8. Normal distribution fits to the PDFs of SLF for ECHAM6, CAM-IMPACT, CAM-OSLO, and CAM5.1 MAM7, for (a) Experiment 1, (b) Experiment 2, and (c) CALIOP.

-0.5 W m^{-2} for CAM5.1 MAM7. Although CAM5.1 MAM7 results in significant changes in the SLF, these changes are not reflected in the radiative properties as much as in CAM-Oslo because the change in total column cloud liquid water mass is a factor of 5 smaller in CAM5.1 MAM7.

To further analyze the differences between the two experiments, we examine the vertical profiles. Figure 5b shows the zonally averaged annual mean number concentrations of particles larger than $0.5 \mu\text{m}$ that can act as IN for all GCMs. The IN concentrations reduce for all GCMs at mixed-phase cloud temperatures. These reductions are significantly larger in ECHAM6, CAM-IMPACT, CAM-Oslo, and SPRINTARS compared to the moderate reductions in CAM5.1. With the limitation of potential IN to particles larger than $0.5 \mu\text{m}$, there is a better consensus among potential IN concentrations in models. Figure 9 shows the zonally averaged annual mean profiles of the same fields as in Figure 6 but for the difference between Experiment 2 and Experiment 1. Consistent with the reduction in IN concentrations (Figure 5b) with the implementation of the fixed ice nucleation mechanism, ice crystal concentrations also reduce for all GCMs (Figure 9a). The reduction in ice crystal number concentration is most pronounced for CAM-Oslo. The reduction in the number of vertically integrated ice crystals is also an order of magnitude larger for CAM-Oslo compared to the other GCMs (Table 4). Similarly, all models simulate some degree of reduction in the mass mixing ratio of ice (Figure 9c). Depending on the model specific relation between the changes in ice crystal number concentration and ice mass mixing ratio, the models simulate either increased or decreased ice crystal sizes. For CAM-Oslo and CAM-IMPACT, the addition of the fixed nucleation mechanism results in greater liquid water mass (Figure 9d) and enhanced cloudiness (Figure 9e) in the regions of reduced ice crystal number concentrations (Figure 9a). Furthermore, in these regions, the ice mass mixing ratio (Figure 9c) is reduced and the ice crystals become larger (Figure 9b). These results are expected because with the reduced number of ice crystals, ice growth

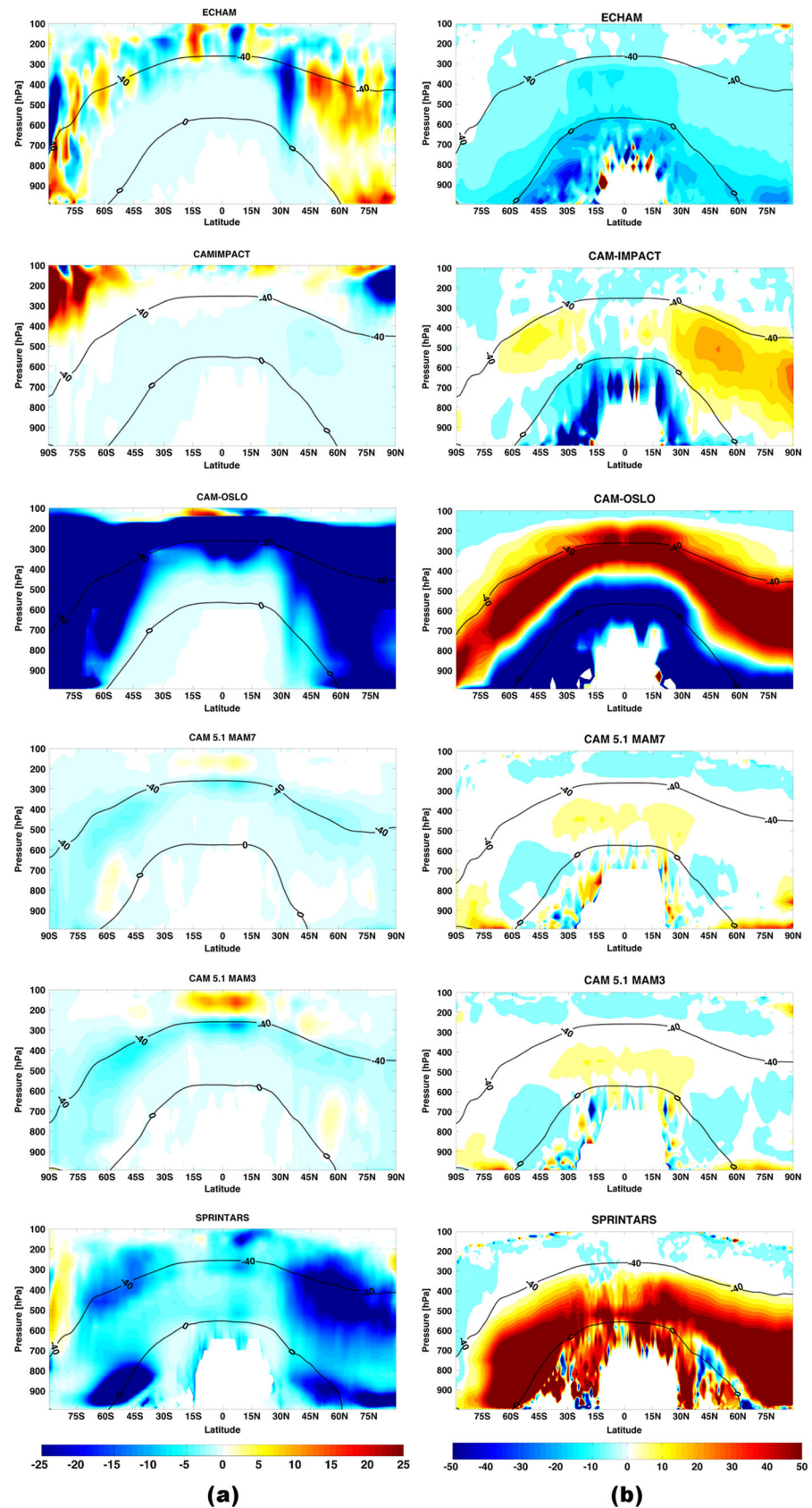


Figure 9

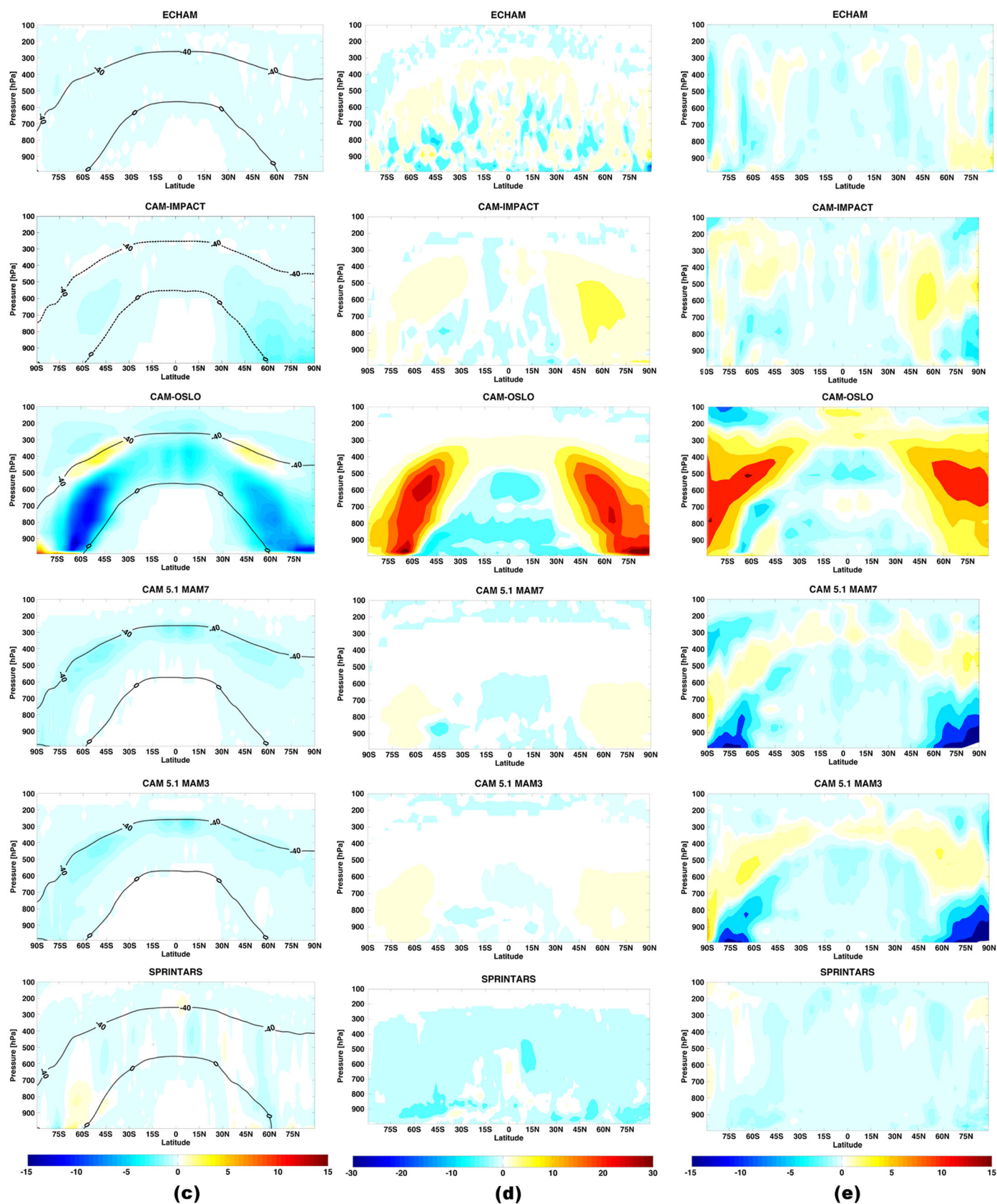


Figure 9. (continued)

rate through the WBF process reduces, which allows for more liquid water to be retained in the clouds leading to fewer and larger crystals. CAM5.1 MAM7 and MAM3 also show similar responses to reduced IN concentrations as CAM-Oslo with smaller magnitudes, which is due to the slower conversion rates through the WBF process [Xie *et al.*, 2013; Liu *et al.*, 2011]. Similarly, for ECHAM6, the reduction of ice crystal number concentrations in Experiment 2 leads to reduced ice water mass (Figure 9c) and enhanced liquid water mass (Figure 9d); however, the response of ice crystal size to changing ice nucleation is not straightforward (Figure 9b). For SPRINTARS, although ice crystal concentrations reduce (Figure 9a) and effective radius increases (Figure 9b) significantly with the fixed nucleation, there is no significant change in cloud ice mass mixing ratio. As a result, along with Figure 9, Table 4 suggests that the cloud ice and liquid water contents are relatively insensitive to changes in ice crystal microphysics for SPRINTARS. The simulated LWP is about a factor of 15 larger than the IWP for both experiments in SPRINTARS (Table 3); therefore, the dominance of the cloud liquid water phase over the cloud ice phase could be a possible reason for the insensitivity to ice processes for SPRINTARS. For ECHAM6, the reduction in IN between the two experiments leads to an increase in cloud liquid water mass (Figures 9b and 9d and Table 3), but the changes in the ice water mass are more modest because less ice mass leads to less precipitation for this GCM (Figure 9c). The change in ice water path for ECHAM6 is smaller than SPRINTARS between the experiments, while the increase in LWP is almost twice as large in the former model (Table 4). Furthermore, when ice nucleation is fixed, cloud droplet number concentrations increase for most models (Table 4), which could influence the cloud water mass and phase partitioning by changing the rate of secondary ice production in some models.

We next examine the changes in cloud heights and cloud radiative properties obtained with the fixed ice nucleation parameterization. For all GCMs, there is an increase in high-level clouds (Figure 9e). For CAM5.1 with both MAM7 and MAM3, cloud fraction increases at the region of reduced cloud ice mass in the upper troposphere (Figure 9e); however, for MAM7, this increase is balanced by the reduction in low-level clouds leading to a small negative change in total cloudiness (Table 4) between the two experiments. Xie *et al.* [2013] provide a detailed analysis on the influence of ice nucleation parameterization in CAM5.1 on cloud fraction and height. For most GCMs, longwave cloud forcing (LWCF) increases in Experiment 2 (Table 4) as a result of the enhanced high-level clouds obtained with the new ice nucleation parameterization and shortwave cloud forcing (SWCF) increases in magnitude due to the overall increase in liquid water paths and cloudiness (Table 4). For CAM5.1 MAM7, there is a reduction in LWCF because of the slight negative change in total cloudiness mentioned above (Table 4). For most GCMs, along with the increase in high-level clouds, there is also a relatively smaller reduction in low-level clouds (Figure 9e). This reduction in low clouds does not take place in CAM-Oslo (Figure 9e). Therefore, the difference between experiments 2 and 1 in the net longwave flux at the surface is positive for CAM-Oslo (Table 4).

We find that replacing the default ice nucleation of the models with a fixed nucleation process leads to fewer IN and in turn ice crystals for all GCMs; however, each model's response to these reductions are different. These results suggest that the differences in the parameterizations of processes subsequent to ice nucleation, such as the ice crystal growth and precipitation used in GCMs could be the more dominant reason for different model responses (i.e., the differences in phase partitioning and cloud water contents). For example, CAM-Oslo uses the vertical velocity criteria on updrafts and downdrafts as explained in Korolev and Mazin [2003] to determine the occurrence of the WBF process using a subgrid scale velocity distribution [Storelvmo *et al.*, 2008b]. This detailed representation allows for more liquid water to be retained in the cloud [Storelvmo *et al.*, 2008b] and could be the reason for the higher SLF obtained in this model and the higher sensitivity to the change in ice nucleation compared to other GCMs. The Korolev and Mazin [2003] approach is also used in ECHAM6; however, there are differences in the implementation. ECHAM6 uses a grid mean vertical velocity along with a turbulent contribution obtained using turbulent kinetic energy and uses only the updraft criterion to determine the occurrence of the WBF process, while CAM-Oslo uses a subgrid scale distribution of the vertical velocity and uses both updraft and downdraft criteria to determine the occurrence of the WBF process. These differences in implementation of the parameterizations along with differences in other

Figure 9. Zonal mean profiles of annual mean difference in (a) ice crystal concentrations (L^{-1}), (b) ice effective radius (μm) (c) cloud ice mass (mg/kg), (d) cloud liquid water mass mixing ratio (mg/kg), and (e) cloud fraction (%) between the two GCM experiments (Experiment 2 – Experiment 1). In a, b and c isotherms of 0 and $-40^{\circ}C$ are plotted to indicate the regions where mixed-phase clouds can occur.

Table 5. Differences in Global Annual Mean Fields Obtained From Multiyear Means Between the Present-Day and Preindustrial (PD-PI) and Between Experiment 2 and Experiment 1 and Their Standard Deviation^a

GCMs	LWP (g m^{-2})	IWP (g m^{-2})	LWCF (W m^{-2})	SWCF (W m^{-2})	CLD (%)	FTOA (W m^{-2})	CF (W m^{-2})
<i>Experiment 1 (PD-PI)</i>							
ECHAM6	5.32 \pm 0.54	0.07 \pm 0.01	0.16 \pm 0.06	−1.15 \pm 0.11	0.25 \pm 0.18	−1.22 \pm 0.18	−0.99 \pm 0.13
CAM-IMPACT	0.61 \pm 1.05	0.75 \pm 0.05	−0.19 \pm 0.07	−0.6 \pm 0.5	−0.09 \pm 0.14	−1.45 \pm 0.41	−0.79 \pm 0.47
CAM-Oslo	1.43 \pm 0.79	0.06 \pm 0.21	−0.06 \pm 0.07	−0.59 \pm 0.41	−0.07 \pm 0.2	−0.49 \pm 0.36	−0.65 \pm 0.43
CAM5.1 MAM7	3.62 \pm 0.12	0.02 \pm 0.14	0.42 \pm 0.05	−1.65 \pm 0.17	0.17 \pm 0.22	−1.62 \pm 0.18	−1.23 \pm 0.14
CAM5.1 MAM3	3.28 \pm 0.46	0.21 \pm 0.06	0.58 \pm 0.08	−1.73 \pm 0.2	0.08 \pm 0.09	−1.34 \pm 0.33	−1.15 \pm 0.26
SPRINTARS	1.15 \pm 1.79	0.05 \pm 0.35	0.23 \pm 0.61	−0.74 \pm 0.43	0.03 \pm 0.32	−0.94 \pm 0.25	−0.51 \pm 0.28
<i>Experiment 2 (PD-PI)</i>							
ECHAM6	5.39 \pm 0.53	0.1 \pm 0.03	0.22 \pm 0.16	−1.26 \pm 0.18	0.22 \pm 0.17	−1.5 \pm 0.09	−1.04 \pm 0.07
CAM-IMPACT	2.83 \pm 1.12	0.38 \pm 0.07	−0.03 \pm 0.07	−1.16 \pm 0.36	−0.03 \pm 0.13	−1.86 \pm 0.48	−1.19 \pm 0.41
CAM-Oslo	2.2 \pm 0.45	−0.03 \pm 0.07	−0.06 \pm 0.06	−0.75 \pm 0.22	0.09 \pm 0.26	−0.81 \pm 0.27	−0.81 \pm 0.20
CAM5.1 MAM7	3.66 \pm 0.21	0.32 \pm 0.17	0.65 \pm 0.15	−1.79 \pm 0.13	0.31 \pm 0.12	−1.51 \pm 0.15	−1.14 \pm 0.1
CAM5.1 MAM3	4.02 \pm 0.59	0.44 \pm 0.22	0.76 \pm 0.16	−2.01 \pm 0.34	0.31 \pm 0.25	−1.44 \pm 0.25	−1.24 \pm 0.25
SPRINTARS	0.48 \pm 1.5	0.1 \pm 0.19	0.27 \pm 0.27	−0.63 \pm 0.41	0 \pm 0.17	−0.91 \pm 0.21	−0.36 \pm 0.19
GCMs	Δ LWP (g m^{-2})	Δ IWP (g m^{-2})	Δ LWCF (W m^{-2})	Δ SWCF (W m^{-2})	Δ CLD (%)	Δ FTOA (W m^{-2})	Δ CF (W m^{-2})
<i>Experiment 2 – Experiment 1 (PD-PI)</i>							
ECHAM6	0.07 \pm 0.75	0.03 \pm 0.03	0.06 \pm 0.15	−0.11 \pm 0.23	−0.03 \pm 0.10	−0.28 \pm 0.20	−0.05 \pm 0.14
CAM-IMPACT	2.22 \pm 1.28	−0.37 \pm 0.09	0.16 \pm 0.04	−0.56 \pm 0.46	0.06 \pm 0.06	−0.41 \pm 0.61	−0.4 \pm 0.42
CAM-Oslo	0.77 \pm 1.21	−0.09 \pm 0.24	0 \pm 0.09	−0.16 \pm 0.54	0.16 \pm 0.32	−0.32 \pm 0.58	−0.16 \pm 0.53
CAM5.1 MAM7	0.04 \pm 0.14	0.3 \pm 0.28	0.23 \pm 0.2	−0.14 \pm 0.23	0.14 \pm 0.22	0.11 \pm 0.11	0.09 \pm 0.09
CAM5.1 MAM3	0.74 \pm 0.87	0.23 \pm 0.24	0.18 \pm 0.17	−0.27 \pm 0.48	0.23 \pm 0.33	−0.11 \pm 0.5	−0.09 \pm 0.49
SPRINTARS	−0.66 \pm 2.12	0.05 \pm 0.28	0.04 \pm 0.43	0.11 \pm 0.47	−0.03 \pm 0.37	0.03 \pm 0.35	0.15 \pm 0.32

^aVariables listed in the table are liquid water path (LWP), ice water path (IWP), longwave cloud forcing (LWCF), shortwave cloud forcing (SWCF), total cloud fraction (CLD), net flux at top of the atmosphere (FTOA), and net cloud forcing (CF). Differences between experiment 2 (PD-PI) and experiment 1 (PD-PI) are given using symbol Δ for all variables.

cloud ice processes could be the reasons for the differences in SLF and sensitivity to ice nucleation between CAM-Oslo and ECHAM6. Furthermore, as hydrometeors grow, the differences in parameterizations such as the autoconversion rates between different hydrometeor categories, the collisional growth rates of hydrometeors, and differences related to the sedimentation of hydrometeors can contribute to the differences in GCM results in both experiments 1 and 2. As explained in section 1, the growth rate through the WBF process, cross-sectional areas for collisional growth parameterizations, and sedimentation rates depend on the shapes that the crystals take as they grow under different environmental conditions. To be able to correctly simulate climate and cloud radiative feedbacks, these processes need to be better formulated in model simulations. Therefore, our results suggest that process level understanding of ice crystals, their nucleation, and growth at various different environmental conditions through in situ and laboratory studies is crucial for improving models. These studies would also benefit satellite retrieval algorithm developments. The information from these studies could be used to reduce the amount of cloud microphysical assumptions made in the retrieval algorithms, i.e., MODIS and ISCCP algorithms. For millimeter wavelength radars such as the one used on CloudSat, it has been shown that determining the distribution of ice mass within different ice crystals is crucial to develop better retrievals, in particular both crystal shape and local distributions of water molecules for each shape influence its scattering properties, which suggest that knowledge of the growth histories of the crystals are important for improving these retrievals [Lu *et al.*, 2013]. For CALIOP, the uncertainties arise largely due to the difficulties in distinguishing the depolarization ratio between the horizontally oriented ice particles and liquid water drops [Hu *et al.*, 2009]. As the crystal orientation may depend on crystal shapes (crystal growth characteristics) and environmental conditions [e.g., Hu *et al.*, 2009], these studies could also improve the phase determination algorithm in CALIOP by providing guidelines for particle orientation under different environmental conditions to prevent misclassification of ice as liquid water.

4.3. Aerosol Effects

The total aerosol effect is obtained using the top of the atmosphere (TOA) radiative flux differences between present-day (PD) and preindustrial (PI) simulations and is presented in Table 5 as the net flux at TOA for all

GCMs for both experiments. For both experiments, the total aerosol effect is a cooling (i.e., a negative radiative forcing) and is the smallest for CAM-Oslo. The mean total aerosol forcing of all GCMs is a cooling of 1.18 W m^{-2} for Experiment 1 and 1.34 W m^{-2} for Experiment 2. Furthermore, the difference in the total aerosol effect between the two experiments offers an insight into the influence of ice nucleation parameterization on the total aerosol effect and is also listed in Table 5. Most GCMs tend to produce more cooling with the fixed ice nucleation in Experiment 2 compared to Experiment 1 as a result of increased liquid water mass, along with cloud fraction except for CAM5.1 MAM7 and SPRINTARS (Table 5). The difference in the total aerosol forcing between the two experiments is small but of opposite signs for CAM5.1 MAM7 compared to MAM3 (Table 5).

The aerosol indirect effect can be inferred from the change (PD-PI) in net cloud radiative forcing, which is the sum of the SWCF and LWCF. In both experiments, the aerosol indirect effect is a cooling of the Earth-atmosphere system for all GCMs (Table 5) with a mean of 0.89 and 0.96 W m^{-2} in Experiments 1 and 2, respectively. Similarly, the difference between Experiments 2 and 1 in the aerosol indirect effect shows the influence of fixing the ice nucleation parameterization on the aerosol indirect effect. The influence of using the *DeMott et al.* [2010] ice nucleation parameterization on the aerosol indirect effect is a cooling for all GCMs except for CAM5.1 MAM7 and SPRINTARS (Table 5). For all GCMs, LWCF is increased (except for CAM-Oslo where there is no change in LWCF) and SWCF is more negative (except for SPRINTARS) in Experiment 2 compared to Experiment 1 (Table 5). The differences presented in Table 5 are generally not statistically significant.

5. Conclusions

In this study, we compared several different GCMs to evaluate the differences in model-simulated cloud ice and liquid water properties and cloud water phase partitioning. The GCMs included in this study can be characterized as state-of-the-art when it comes to the representation of cloud ice microphysics in global models. Despite their detailed cloud microphysics and aerosol treatment, all GCMs compared in this study are underestimating the IWP and overestimating the LWP with varying degrees of magnitude compared to satellite observations. Furthermore, they produce dramatically different phase partitioning at the isotherms considered compared to each other, and none of them are capable of reproducing the phase partitioning of cloud water as observed by CALIOP. Although some GCMs produced large LWPs that are comparable to observations, they also retained very small fraction of supercooled liquid water at mixed-phase temperatures. Consequently, our results show that it is important to evaluate the GCMs based on vertical profiles of water contents when validating their ability to simulate climate rather than comparing the integrated amount of water in the simulated atmospheric column, as done in most comparison/validation studies.

With the results of Experiment 1, we see that the different GCM aerosol schemes along with different characterizations of IN in each GCM lead to different numbers of potential ice nuclei, but that the concentration of potential IN alone is not a good predictor of ice crystal concentrations. The ice nucleation parameterization in the models determines what fraction of the available IN is nucleated under certain environmental conditions. As a result, cloud properties such as the liquid and ice water mass and ice crystal radius simulated in different models are different. Furthermore, with the results of Experiment 2, we find that these differences do not reduce with the use of the fixed ice nucleation mechanism in all GCMs. The reduction in ice crystal number concentrations with the fixed ice nucleation mechanism leads to different responses in each model depending on the parameterized processes subsequent to ice nucleation, i.e., the model's ice crystal growth and precipitation microphysics. These results underline the importance of cloud ice processes in determining cloud water phase and water contents. For future modeling studies, it would be interesting to carry out additional sensitivity studies to explore the relative contributions of cloud ice processes to cloud water phase, concentrating on the GCM parameterizations of growth through the WBF process and collection, autoconversion, and precipitation.

We also find that cloud water phase is sensitive to the simulated ratio of column-integrated liquid water mass to ice water mass. GCMs that have a smaller difference in magnitude between their simulated LWP and IWP (i.e., LWP is less than a factor of ~ 3 larger than the IWP), such as CAM-Oslo and CAM5.1, are more sensitive to the changes in the ice nucleation parameterization, especially the phase partitioning of cloud water. While for other GCMs with larger simulated LWPs compared to IWP (ECHAM6, CAM-IMPACT, and SPRINTARS), there is a lower sensitivity to changes in the ice nucleation parameterization. Furthermore, the high sensitivity to

the change in ice nucleation in CAM-Oslo is reflected in both water paths and in the partitioning of the cloud water phase (SLF), while for CAM5.1 MAM7, a high sensitivity is observed in the SLF only. The changes in SLF are not reflected to radiative properties in CAM5.1 MAM7 as much as CAM-Oslo, because the change in total column cloud liquid water mass is a factor of 5 larger in CAM-Oslo.

Our results suggest that LWP (IWP) is overestimated (underestimated) in all models and cases presented in this study compared to satellite observations and that the spatial distribution and magnitude of the simulated SLF is different among the six GCMs and compared to the retrievals from CALIOP for both cases studied. One way to match the observed cloud phase partitioning would be to prescribe the SLF from CALIOP observations. This is beyond the scope of this study but would be an interesting study to carry out in the future. Nonetheless, our results show that at temperature ranges that allow for mixed-phase clouds, the cloud top SLF from CALIOP is much larger compared to the SLF from the GCMs. These results indicate that prescribing the SLF from CALIOP could decrease the already underpredicted IWP and increase the overpredicted LWP of the GCMs. We conclude that rather than forcing the GCMs to agree with one specific satellite retrieval (the SLF), the way forward goes via improved representation of cloud ice processes that may eventually reduce the discrepancies between the modeled and observed cloud water contents and SLF simultaneously.

With Experiment 2, we found that cloud ice processes subsequent to nucleation are at least as important in terms of the phase partitioning of cloud water. Therefore, we suggest that in addition to a good representation of ice nucleation, it is also crucial for GCMs to accurately represent the growth characteristics of ice crystals under various conditions and their sedimentation to be able to capture the observed SLF and vertical profiles of ice and liquid water contents. Furthermore, we show that the ability of satellite retrievals to accurately determine cloud water phase as a function of height or temperature is crucial for their usefulness in validations of model-simulated mixed-phase clouds. Because satellite retrieval algorithms and in turn retrieved water contents are sensitive to the growth and sedimentation characteristics of the hydrometeors, it is essential to improve the process level understanding of cloud ice to obtain retrievals more representative of the actual vertical profiles of cloud properties that can be used for model validation and parameterization development. Hence, our results reveal that future field campaigns and laboratory studies dedicated to understanding ice formation, growth, and precipitation in clouds will be crucial for improved process level understanding. Such studies will ultimately improve both modeling and satellite retrieval studies and in turn climate predictions. To be able to effectively use retrievals such as CALIOP for model validation/improvement, future field studies are needed to validate these retrievals and determine the uncertainties in them. Modeling studies to test the performance of parameterizations developed based on the observational results and to reduce the deficiencies of the subgrid scale representation of these processes are also needed for improved representation of cloud processes in the models. Adequate representations of these processes in GCMs are crucial for their ability to accurately predict the cloud water contents, number concentrations, cloud particle sizes, and hence cloud forcing, cloud feedback, and the warming on the Earth's surface for the various future emission scenarios. Ultimately, simulated aerosol forcings and cloud-climate feedbacks rely on the improved representation of cloud processes. Uncertainties in climate forcings and feedback mechanisms are currently preventing us from producing more informed climate projections of global warming.

Acknowledgments

M. Komurcu would like to acknowledge David M. Winker, Steven Platnick, and Robert Pincus for treasured discussions regarding the uncertainties in satellite retrievals and Eugene E. Clothiaux and Jerry Y. Harrington for providing valuable comments on the influence of crystal habit in retrieval algorithms. This work was supported in part by the facilities and staff of the Yale University Faculty of Arts and Sciences High Performance Computing Center. X. Liu and Y. Wang thank the support by the DOE's Office of Science/Biological and Environmental Research, through Earth System Modeling Program. PNNL is operated for DOE by Battelle Memorial Institute under contract DE-AC06-76RLO 1830. T. Takemura is supported by the Funding Program for Next Generation World-Leading Researchers of the Cabinet Office, Government of Japan (GR079). U. Lohmann would like to acknowledge support from the BACCHUS EU FP7-603445 project. We also would like to thank the anonymous reviewers, whose valuable comments helped to clarify and improve the paper. Satellite retrievals used in this study and described in section 2 are available online. CALIOP retrievals can be downloaded from <https://eosweb.larc.nasa.gov/order-data>. NCEP Reanalysis-2 products are available online at <http://www.esrl.noaa.gov/psd/data/gridded/data.ncep.reanalysis2.pressure.html>. MODIS LWP and IWP data products are available online at <http://ladsweb.nascom.nasa.gov/data/search.html>. CloudSat IWP products are available online at <http://www.cloudsat.cira.colostate.edu>. ISCCP LWP and IWP products are available online from different providers listed in the project description website: <http://isccp.giss.nasa.gov/products/obtaining.html>

References

- Austin, R. T., A. J. Heymsfield, and G. L. Stephens (2009), Retrieval of ice cloud microphysical parameters using the CloudSat millimeter-wave radar and temperature, *J. Geophys. Res.*, *114*, D00A23, doi:10.1029/2008JD010049.
- Avramov, A., and J. Y. Harrington (2010), The influence of parameterized ice habit on simulated mixed-phase Arctic clouds, *J. Geophys. Res.*, *115*, D03205, doi:10.1029/2009JD012108.
- Bergeron, T. (1935), On the physics of clouds and precipitation, in *Proces Verbaux de l'Association de Météorologie*, pp. 156–178, International Union of Geodesy and Geophysics, Paris, Fr.
- Choi, Y., C. H. Ho, S. W. Kim, and R. S. Lindzen (2010), Observational diagnosis of cloud phase in the winter Antarctic atmosphere for parameterizations in climate models, *Adv. Atmos. Sci.*, *27*(6), 1233–1245, doi:10.1007/s00376-010-9175-3.
- Cotton, W. R., G. J. Tripoli, R. M. Rauber, and E. A. Mulvihill (1986), Numerical simulation of the effects of varying ice crystal nucleation rates and aggregation processes on orographic snowfall, *J. Climate Appl. Meteorol.*, *25*, 1658–1680, doi:10.1175/1520-0450(1986)025%3C1658: NSOTEO%3E2.0.CO;2.
- DeMott, P. J., A. J. Prenni, X. Liu, S. M. Kreidenweis, M. D. Petters, C. H. Twohy, M. S. Richardson, T. Eidhammer, and D. C. Rogers (2010), Predicting global atmospheric ice nuclei distributions and their impacts on climate, *Proc. Natl. Acad. Sci. U.S.A.*, *107*(25), 11,217–11,222, doi:10.1073/pnas.0910818107.
- DeMott, P. J., et al. (2011), Resurgence in ice nucleation research, *Bull. Am. Meteorol. Soc.*, *92*, 1623–1635, doi:10.1175/2011BAMS3119.1.
- Dentener, F., et al. (2006), Emissions of primary aerosol and precursor gases in the years 2000 and 1750 prescribed data-sets for AeroCom, *Atmos. Chem. Phys.*, *6*, 4321–4344, doi:10.5194/acp-6-4321-2006.

- Diehl, K., M. Simmel, and S. Wurzler (2006), Numerical sensitivity studies on the impact of aerosol properties and drop freezing modes on the glaciation, microphysics, and dynamics of clouds, *J. Geophys. Res.*, **111**, D07202, doi:10.1029/2005JD005884.
- Eliasson, S., S. A. Buehler, M. Milz, P. Eriksson, and V. O. John (2011), Assessing observed and modelled spatial distributions of ice water path using satellite data, *Atmos. Chem. Phys.*, **11**, 375–391, doi:10.5194/acp-11-375-2011.
- Fan, J., S. Ghan, M. Ovchinnikov, X. Liu, P. J. Rasch, and A. Korolev (2011), Representation of Arctic mixed-phase clouds and the Wegener-Bergeron-Findeisen process in climate models: Perspectives from a cloud-resolving study, *J. Geophys. Res.*, **116**, D00T07, doi:10.1029/2010JD015375.
- Findeisen, W. (1938), Kolloid-meteorologische Vorgänge bei Neiderschlags-bildung, *Meteorol. Z.*, **55**, 121–133.
- Fridlind, A. M., et al. (2012), A comparison of TWP-ICE observational data with cloud-resolving model results, *J. Geophys. Res.*, **117**, D05204, doi:10.1029/2011JD016595.
- Fukuta, N., and T. Takahashi (1999), The growth of atmospheric ice crystals: A summary of findings in vertical supercooled cloud tunnel studies, *J. Atmos. Sci.*, **56**, 1963–1979, doi:10.1175/1520-0469(1999)056<1963:TGOAIC>2.0.CO;2.
- Gettelman, A., X. Liu, S. J. Ghan, H. Morrison, S. Park, and A. J. Conley (2010), Global simulations of ice nucleation and ice supersaturation with an improved cloud scheme in the Community Atmospheric Model, *J. Geophys. Res.*, **115**, D18216, doi:10.1029/2009JD013797.
- Gettelman, A., X. Liu, D. Barahona, U. Lohmann, and C. Chen (2012), Climate impacts of ice nucleation, *J. Geophys. Res.*, **117**, D20201, doi:10.1029/2012JD017950.
- Han, Q., W. B. Rossow, J. Chou, and R. M. Welch (1998), Global variations of column droplet concentration in low-level clouds, *Geophys. Res. Lett.*, **25**, 1419–1422, doi:10.1029/98GL01095.
- Heymsfield, A. J., et al. (2008), Testing IWC retrieval methods using radar and ancillary measurements with in situ data, *J. Appl. Meteorol. Climatol.*, **47**(1), 135–163, doi:10.1175/2007JAMC1606.1.
- Hoose, C., J. E. Kristjánsson, J. P. Chen, and A. Hazra (2010), A classical-theory-based parameterization of heterogeneous ice nucleation by mineral dust, soot, and biological particles in a global climate model, *J. Atmos. Sci.*, **67**, 2483–2503, doi:10.1175/2010JAS3425.1.
- Hu, Y., et al. (2009), CALIPSO/CALIP cloud phase discrimination algorithm, *J. Atmos. Oceanic Technol.*, **26**, 2293–2309, doi:10.1175/2009JTECHA1280.1.
- Hubanks, P. A., M. D. King, S. A. Platnick, and R. A. Pincus (2008), MODIS Atmospheric L3 gridded product algorithm theoretical basis document ATBD-MOD-30, Goddard Space Flight Cent., Greenbelt, Md.
- Hunt, W. H., D. M. Winker, M. A. Vaughan, K. A. Powell, P. L. Luckner, and C. Weimer (2009), CALIPSO lidar description and performance assessment, *J. Atmos. Oceanic Technol.*, **26**, 1214–1228, doi:10.1175/2009JTECHA1223.1.
- Intergovernmental Panel on Climate Change (2013), Chapter 7 of the fifth assessment report of the Intergovernmental Panel on Climate Change. [Available at http://www.climatechange2013.org/images/uploads/WGIAR5_WGI-12Doc2b_FinalDraft_Chapter07.pdf.]
- Jiang, J. H., et al. (2012), Evaluation of cloud and water vapor simulations in CMIP5 climate models using NASA "A-Train" satellite observations, *J. Geophys. Res.*, **117**, D14105, doi:10.1029/2011JD017237.
- Kanamitsu, M., W. Ebisuzaki, J. Woollen, S.-K. Yang, J. J. Hnilo, M. Fiorino, and G. L. Potter (2002), NCEP–DOE AMIP-II Reanalysis (R-2), *Bull. Am. Meteorol. Soc.*, **83**, 1631–1643, doi:10.1175/BAMS-83-11-1631.
- King, M. D., W. P. Menzel, Y. J. Kaufman, D. Tanre, B.-C. Gao, S. Platnick, S. A. Ackerman, L. A. Remer, R. Pincus, and P. A. Hubanks (2003), Cloud and aerosol properties, precipitable water, and profiles of temperature and water vapor from MODIS, *IEEE Trans. Geosci. Remote Sens.*, **41**(2), 442–458, doi:10.1109/TGRS.2002.808226.
- Komurcu, M., T. Storelvmo, I. Tan, U. Lohmann, Y. Yun, J. E. Penner, Y. Wang, X. Liu, and T. Takemura (2013), Inter-comparison of the phase partitioning of cloud water among global climate models, International Conference on Nucleation and Atmospheric Aerosols (ICNAA), *AIP Conf. Proc.*, **1527**, 755–758, doi:10.1063/1.4803381.
- Korolev, A. V., and I. P. Mazin (2003), Supersaturation of water vapor in clouds, *J. Atmos. Sci.*, **60**, 2957–2974, doi:10.1175/1520-0469(2003)060<2957:SOWVIC>2.0.CO;2.
- Lamarque, J.-F., et al. (2010), Historical (1850–2000) gridded anthropogenic and biomass burning emissions of reactive gases and aerosols: Methodology and application, *Atmos. Chem. Phys.*, **10**, 7017–7039, doi:10.5194/acp-10-7017-2010.
- Lebsock, M. D., T. S. L'ecuyer, and G. L. Stephens (2011), Detecting the ratio of rain and cloud water in low-latitude shallow marine clouds, *J. Appl. Meteorol. Climatol.*, **50**(2), 419–432, doi:10.1175/2010JAMC2494.1.
- Levkov, L., B. Rockel, H. Kapitzka, and E. Raschke (1992), 3D mesoscale numerical studies of cirrus and stratus clouds by their time and space evolution, *Beitr. Phys. Atmos.*, **65**, 35–58, doi:10.5194/acp-13-9021-2013.
- Li, Z.-X., and H. Le Treut (1992), Cloud-radiation feedbacks in a general circulation model and their dependence on cloud modeling assumptions, *Clim. Dyn.*, **7**, 133–139, doi:10.1007/BF00211155.
- Lin, B., and W. B. Rossow (1996), Seasonal variation of liquid and ice water path in nonprecipitating clouds over oceans, *J. Clim.*, **9**, 2890–2902, doi:10.1175/1520-0442(1996)009<2890:SVOLAI>2.0.CO;2.
- Liu, X., J. E. Penner, and M. Herzog (2005), Global modeling of aerosol dynamics: Model description, evaluation, and interactions between sulfate and nonsulfate aerosols, *J. Geophys. Res.*, **110**, D18206, doi:10.1029/2004JD005674.
- Liu, X., J. E. Penner, S. J. Ghan, and M. Wang (2007), Inclusion of ice microphysics in the NCAR Community Atmospheric Model version 3 (CAM3), *J. Clim.*, **20**, 4526–4547, doi:10.1175/JCLI4264.1.
- Liu, Z., M. Vaughan, D. Winker, C. Kittaka, B. Getzewich, R. Kuehn, A. Omar, K. Powell, C. Trepte, and C. Hostetler (2009), The CALIPSO lidar cloud and aerosol discrimination: Version 2 algorithm and initial assessment of performance, *J. Atmos. Oceanic Technol.*, **26**, 1198–1213, doi:10.1175/2009JTECHA1229.1.
- Liu, X., et al. (2011), Testing cloud microphysics parameterizations in NCAR CAM5 with ISDAC and M-PACE observations, *J. Geophys. Res.*, **116**, D00T11, doi:10.1029/2011JD015889.
- Liu, X., et al. (2012), Toward a minimal representation of aerosols in climate models: Description and evaluation in the Community Atmosphere Model CAM5, *Geosci. Model Dev. Discuss.*, **5**, 709–739, doi:10.5194/gmd-5-709-2012.
- Loeb, N. G., B. A. Wielicki, D. R. Doelling, G. L. Smith, D. F. Keyes, S. Kato, N. Manalo-Smith, and T. Wong (2009), Toward optimal closure of the Earth's top-of-atmosphere radiation budget, *J. Clim.*, **22**, 748–766, doi:10.1175/2008JCLI2637.1.
- Lohmann, U., and K. Diehl (2006), Sensitivity studies of the importance of dust ice nuclei for the indirect aerosol effect on stratiform mixed-phase clouds, *J. Atmos. Sci.*, **63**, 968–982, doi:10.1175/JAS3662.1.
- Lohmann, U., and C. Hoose (2009), Sensitivity studies of different aerosol indirect effects in mixed-phase clouds, *Atmos. Chem. Phys.*, **9**, 8917–8934, doi:10.5194/acp-9-8917-2009.
- Lohmann, U., P. Stier, C. Hoose, S. Ferrachat, S. Kloster, E. Roeckner, and J. Zhang (2007), Cloud microphysics and aerosol indirect effects in the global climate model ECHAM5-HAM, *Atmos. Chem. Phys.*, **7**(3425–3446), 2007, doi:10.5194/acp-7-3425-2007.
- Lu, Y., E. E. Clothiaux, K. Aydin, G. Botta, and J. Verlinde (2013), Modeling variability in dendritic ice crystal backscattering cross sections at millimeter wavelengths using a modified Rayleigh-Gans theory, *J. Quant. Spectrosc. Radiat. Transfer*, **131**, 95–104, doi:10.1016/j.jqsrt.2013.05.008.
- McFarquhar, G. M., et al. (2011), Indirect and semi-direct aerosol campaign, *Bull. Am. Meteorol. Soc.*, **92**, 183–201, doi:10.1175/2010BAMS2935.1.

- Menon, S., et al. (2003), Evaluating aerosol/cloud/radiation process parameterizations with single-column models and Second Aerosol Characterization Experiment (ACE-2) cloudy column observations, *J. Geophys. Res.*, *108*(D24), 4762, doi:10.1029/2003JD003902.
- Meyers, M. P., P. J. DeMott, and W. R. Cotton (1992), New primary ice-nucleation parameterizations in an explicit cloud model, *J. Appl. Meteorol.*, *31*, 708–721, doi:10.1175/1520-0450(1992)031<0708:NPINPI>2.0.CO;2.
- Mitchell, J. F. B., C. A. Senior, and W. J. Ingram (1989), CO₂ and climate: A missing feedback?, *Nature*, *341*, 132–134, doi:10.1038/341132a0.
- Morrison, H., and A. Gettelman (2008), A new two-moment bulk stratiform cloud microphysics scheme in the NCAR Community Atmosphere Model (CAM3). Part I: Description and numerical tests, *J. Clim.*, *21*(15), 3642–3659, doi:10.1175/2008JCLI2105.1.
- Omar, A. H., et al. (2009), The CALIPSO automated aerosol classification and lidar ratio selection algorithm, *J. Atmos. Oceanic Technol.*, *26*, 1994–2014, doi:10.1175/2009JTECHA1231.1.
- Penner, J. E., J. Quaas, T. Storelvmo, T. Takemura, O. Boucher, H. Guo, A. Kirkevåg, J. E. Kristjánsson, and Ø. Seland (2006), Model intercomparison of indirect aerosol effects, *Atmos. Chem. Phys.*, *6*, 3391–3405, doi:10.5194/acp-6-3391-2006.
- Phillips, V. T. K., P. J. DeMott, and C. Andronache (2008), An empirical parameterization of heterogeneous ice nucleation for multiple chemical species of aerosols, *J. Atmos. Sci.*, *65*(9), 2757–2783, doi:10.1175/2007JAS2546.1.
- Platnick, S., R. Pincus, B. Wind, M. D. King, M. A. Gray, and P. Hubanks (2004), An initial analysis of the pixel-level uncertainties in global MODIS cloud optical thickness and effective particle size retrievals, in *Passive Optical Remote Sensing of the Atmosphere and Clouds IV*, Proceedings of the SPIE, vol. 5652, edited by S. C. Tsay, T. Yokota, and M.-H. Ahn, pp. 30–40, doi:10.1117/12.578353. [Available at http://spie.org/x648.html?product_id=578353.]
- Pruppacher, H. R., and J. D. Klett (1997), *Microphysics of Clouds and Precipitation*, 2nd ed., Kluwer Academic Publishers, Boston, MA, isbn: 0-7923-4211-9.
- Quaas, J., et al. (2009), Aerosol indirect effects—General circulation model intercomparison and evaluation with satellite data, *Atmos. Chem. Phys.*, *9*, 8697–8717, doi:10.5194/acp-9-8697-2009.
- Rossow, W. B., and R. A. Schiffer (1999), Advances in understanding clouds from ISCCP, *Bull. Am. Meteorol. Soc.*, *80*, 2261–2287, doi:10.1175/1520-0477(1999)080<2261:AIUCFI>3.0.CO;2.
- Rotstain, L. D., B. F. Ryan, and J. J. Katzfey (2000), A scheme for calculation of the liquid fraction in mixed-phase stratiform clouds in large-scale models, *Mon. Weather Rev.*, *128*, 1070–1088, doi:10.1175/1520-0493(2000)128<1070:ASFCOT>2.0.CO;2.
- Seland, Ø., T. Iversen, A. Kirkevåg, and T. Storelvmo (2008), Aerosol-climate interactions in the CAM-Oslo atmospheric GCM and investigation of associated basic shortcomings, *Tellus A*, *60*, 459–491, doi:10.1111/j.1600-0870.2008.00318.x.
- Stephens, G. L., et al. (2002), The CloudSat mission and the A-Train, *Bull. Am. Meteorol. Soc.*, *83*, 1771–1790, doi:10.1175/BAMS-83-12-1771.
- Stephens, G. L., J. Li, M. Wild, C. A. Clayson, N. Loeb, S. Kato, T. L'Ecuyer, P. W. Stackhouse Jr., M. Lebsock, and T. Andrews (2012), An update on Earth's energy balance in light of the latest global observations, *Nat. Geosci.*, *5*, 691–696, doi:10.1038/ngeo1580.
- Stevens, B., et al. (2013), Atmospheric component of the MPI-M Earth System Model: ECHAM6, *J. Adv. Model. Earth Syst.*, *5*, 146–172, doi:10.1002/jame.20015.
- Stier, P., et al. (2005), The aerosol-climate model ECHAM5-HAM, *Atmos. Chem. Phys.*, *5*, 1125–1156, doi:10.5194/acp-5-1125-2005.
- Storelvmo, T., J. E. Kristjánsson, S. J. Ghan, A. Kirkevåg, Ø. Seland, and T. Iversen (2006), Predicting cloud droplet number concentration in Community Atmosphere Model (CAM)-Oslo, *J. Geophys. Res.*, *111*, D24208, doi:10.1029/2005JD006300.
- Storelvmo, T., J. E. Kristjánsson, and U. Lohmann (2008a), Aerosol influence on mixed-phase clouds in CAM-Oslo, *J. Atmos. Sci.*, *65*, 3214–3230, doi:10.1175/2008JAS2430.1.
- Storelvmo, T., J. E. Kristjánsson, U. Lohmann, T. Iversen, A. Kirkevåg, and Ø. Seland (2008b), Modeling of the Wegener-Bergeron-Findeisen process—Implications for aerosol indirect effects, *Environ. Res. Lett.*, *3*, 045001, doi:10.1088/1748-9326/3/4/045001.
- Storelvmo, T., J. E. Kristjánsson, U. Lohmann, T. Iversen, A. Kirkevåg, and Ø. Seland (2010), Correction to modeling the Wegener-Bergeron-Findeisen process—Implications for aerosol indirect effects, *Env. Res. Lett.*, *5*, 019801, doi:10.1088/1748-9326/5/1/019801.
- Storelvmo, T., C. Hoose, and P. Eriksson (2011), Global modeling of mixed-phase clouds: The albedo and lifetime effects of aerosols, *J. Geophys. Res.*, *116*, D05207, doi:10.1029/2010JD014724.
- Takemura, T., H. Okamoto, Y. Maruyama, A. Numaguti, A. Higurashi, and T. Nakajima (2000), Global three-dimensional simulation of aerosol optical thickness distribution of various origins, *J. Geophys. Res.*, *105*(D14), 17,853–17,873, doi:10.1029/2000JD900265.
- Takemura, T., T. Nakajima, O. Dubovik, B. N. Holben, and S. Kinne (2002), Single-scattering albedo and radiative forcing of various aerosol species with a global three-dimensional model, *J. Clim.*, *15*, 333–352, doi:10.1175/1520-0442(2002)015<0333:SSAARF>2.0.CO;2.
- Takemura, T., T. Nozawa, S. Emori, T. Y. Nakajima, and T. Nakajima (2005), Simulation of climate response to aerosol direct and indirect effects with aerosol transport-radiation model, *J. Geophys. Res.*, *110*, D02202, doi:10.1029/2004JD005029.
- Takemura, T., M. Egashira, K. Matsuzawa, H. Ichijo, R. Oishi, and A. Abe-Ouchi (2009), A simulation of the global distribution and radiative forcing of soil dust aerosols at the Last Glacial Maximum, *Atmos. Chem. Phys.*, *9*, 3061–3073, doi:10.5194/acp-9-3061-2009.
- Trenberth, K. E., J. T. Fasullo, and J. Kiehl (2009), Earth's global energy budget, *Bull. Am. Meteorol. Soc.*, *90*, 311–323, doi:10.1175/2008BAMS2634.1.
- Waliser, D., et al. (2009), Cloud ice: A climate model challenge with signs and expectations of progress, *J. Geophys. Res.*, *114*, D00A21, doi:10.1029/2008JD010015.
- Wang, M., J. E. Penner, and X. Liu (2009), The coupled IMPACT aerosol and NCAR CAM3 model: Evaluation of predicted aerosol number and size distribution, *J. Geophys. Res.*, *114*, D06302, doi:10.1029/2008JD010459.
- Warren, S. G., C. J. Hahn, J. London, R. M. Chervin, and R. L. Jenne (1988), *Global Distribution of Total Cloud Cover and Cloud Type Amounts Over the Ocean*, NCAR Tech. Note NCAR/TN-317 + STR, Natl. Cent. for Atmos. Res., Boulder, Colo.
- Wegener, A. (1911), *Thermodynamik der Atmosphäre*, 331 pp., Leipzig.
- Wilson, D. R., and S. P. Ballard (1999), A microphysically based precipitation scheme for the UK meteorological office unified model, *Q. J. R. Meteorol. Soc.*, *125*, 1607–1636, doi:10.1002/qj.49712555707.
- Winker, D. M., M. A. Vaughan, A. Omar, Y. Hu, K. A. Powell, Z. Liu, W. H. Hunt, and S. A. Young (2009), Overview of the CALIPSO mission and CALIOP data processing algorithms, *J. Atmos. Oceanic Technol.*, *26*, 2310–2323, doi:10.1175/2009JTECHA1281.1.
- Xie, S., X. Liu, C. Zhao, and Y. Zhang (2013), Sensitivity of CAM5 simulated Arctic clouds and radiation to ice nucleation parameterization, *J. Clim.*, *26*, 5981–5999, doi:10.1175/JCLI-D-12-00517.1.
- Young, K. C. (1974), The role of contact nucleation in ice phase initiation in clouds, *J. Atmos. Sci.*, *31*, 768–776, doi:10.1175/1520-0469(1974)031<0768:TROCN>2.0.CO;2.
- Yun, Y., and J. E. Penner (2012), Global model comparison of heterogeneous ice nucleation parameterizations in mixed phase clouds, *J. Geophys. Res.*, *117*, D07203, doi:10.1029/2011JD016506.
- Yun, Y., and J. E. Penner (2013), An evaluation of the potential radiative forcing an climatic impact of marine organic aerosols as heterogeneous ice nuclei, *Geophys. Res. Lett.*, *40*, 4121–4126, doi:10.1002/grl.50794.
- Yun, Y., J. E. Penner, and O. Popovicheva (2013), The effects of hygroscopicity of fossil fuel combustion aerosols on mixed-phase clouds, *Atmos. Chem. Phys.*, *13*, 4339–4348, doi:10.5194/acp-13-4339-2013.